



1
2
3
4
5
6
7
8
9
10
11
12
13
14
15
16
17
18
19
20
21
22
23
24
25
26
27
28
29
30
31
32
33
34
35
36
37
38
39
40
41
42
43

A Skewed perspective of the Indian rainfall-ENSO Relationship

Justin Schulte^{1*}, Fredrick Policelli², and Benjamin Zaitchik³

1. Science Systems and Applications, Inc.

2. NASA Goddard Space Flight Center

3. John Hopkins University

*corresponding Author: Justin Schulte (justin.a.schulte@nasa.gov)

Abstract

The application of higher-order wavelet analysis to India rainfall and the El Niño/Southern Oscillation (ENSO) is presented. An auto-bicoherence analysis is used to extract the frequency modes contributing to the skewness of India rainfall and ENSO. A nonlinear wavelet coherence method is proposed for diagnosing why the time-domain correlation between two time series temporally changes when at least one time series has changing nonlinear characteristics.

The results indicate the India rainfall and ENSO are highly nonlinear phenomenon. It is also demonstrated that the sea surface temperature (SST) patterns associated with different nonlinear ENSO modes depend on the frequency components participating in the nonlinear phase coupling. The SST pattern associated with coupling between ENSO modes with periods of 31 and 15.5 months is reminiscent of a central Pacific El Niño and intensifies around 1995, contrasting with the coupling between the 62- and 31- month modes that became active around the 1970s ENSO regime shift. A nonlinear coherence analysis showed that the skewness of India rainfall is weakly correlated with that of 4 ENSO time series after the 1970s, indicating that increases in ENSO skewness after 1970's at least partially contributed to the weakening India rainfall-ENSO relationship in recent decades. The implication of this result is that the intensity of skewed El Niño events is likely to overestimate India drought severity, which was the case in the 1997 monsoon season, a time point when the nonlinear wavelet coherence between All-India rainfall and ENSO reached its lowest value in the 1871-2016 period.

1. Introduction

Precipitation variability across India is largely related to the seasonal Southwest and Northeast monsoon systems involving changes in the prevailing low-level wind direction. Understanding the precipitation variability across India is complex because India rainfall is a non-stationary, non-linear phenomenon that is influenced by numerous large-scale climate patterns such as the El Niño/Southern Oscillation (ENSO; Walker and Bliss, 1932) and the Indian Ocean Dipole (IOD; Ashok et al., 2001; Ashok et al., 2004) pattern. Predicting India rainfall has important implications for the agriculture, human health, and economy of India, making the Indian monsoon an active area of research despite early work on monsoon prediction extending back to the 1800s (Blanford, 1884).

An important source of predictability for the Indian monsoon is ENSO. During EL Niño years, droughts are favored, while rainfall surpluses are favored during La Niña years. However, there is no one-to-one relationship between ENSO and Indian rainfall. As a result, summer rainfall predictions based on ENSO have proven challenging. For example, the 1997/1998 EL Niño event was extremely strong yet climatological Indian monsoon conditions were observed (Shen and Kimoto, 1999; Slingo and Annamalai, 2000). It is therefore important to understand why certain El Niño events are not accompanied by monsoon failures.

There are a few reasons for the challenges faced when predicting Indian rainfall using ENSO. The first reason is that the relationship between ENSO and India rainfall is non-stationary. As shown by Torrence and Webster (1999), the relationship between ENSO and India rainfall cycles between periods of high and low coherence. Kumar et al. (1999) found that the relationship between India rainfall and ENSO weakened in the 1970s and hypothesized that a southward shift in Walker circulation anomalies associated with ENSO events and increased Eurasian spring and winter surface temperatures was responsible for the weakening relationship. Other work suggests that the changing



44 ENSO-India rainfall relationship was the result of tropical Atlantic sea surface temperatures (SSTs) and the Atlantic
45 Multi-decadal Oscillation modulating the relationship (Lu et al., 2006; Kucharski et al. 2007; Kucharski et al., 2009;
46 Chen et al., 2010). In contrast, Kumar et al (2006) and Fan et al. (2017) argued that the occurrence of different ENSO
47 flavors (Johnson, 2013) such as the Eastern Pacific and Central Pacific types could explain the changes in the ENSO-
48 India rainfall relationship. Other investigators adopted another perspective to explain changes in the ENSO-India
49 rainfall relationship and concluded that temporal undulations in the ENSO-India rainfall relationship are related to
50 statistical under sampling and stochastic fluctuations (Gershunov et al. 2001; van Oldenborgh and Burgers, 2005;
51 Delsole and Shukla, 2006; Cash et al., 2017). In a recent analysis, Yun and Timmermann (2018) showed that changes
52 in the ENSO-Indian rainfall relationship are consistent with a stochastically perturbed ENSO signal and argued that
53 changes in the ENSO-India monsoon relationship may not be related to external climate forcing mechanisms.

54 The second reason for the ENSO-related prediction challenges is that ENSO itself is a non-stationary
55 phenomenon. Using wavelet analysis, Kestin et al. (1998) found that the interannual variability of ENSO from 1930
56 to 1960 was dominated by a 4- to 7- year periodicity, whereas for the time period from 1960 to 1990, the interannual
57 variability was also dominated by a 2- to 5- year periodicity. A wavelet power spectral analysis conducted by Torrence
58 and Webster (1999) and Schulte (2016a) showed that ENSO signal energy in the 2- to 7-year period band undulates,
59 with the signal energy of the Niño 3.4 time series particularly pronounced after the 1960s (Schulte 2016a).

60 The nonlinear characteristics (e.g. skewness) of ENSO are also non-stationary and undergo interdecadal
61 changes (Wu and Hsieh, 2003). Numerous studies have reported an ENSO regime shift in the 1970s in which ENSO
62 began to evolve more nonlinearly than in previous decades (An, 2004; An and Jin 2004; An, 2009). It is a curious fact
63 that the ENSO regime shift of the 1970s coincided with the weakening ENSO-India rainfall relationship as
64 documented by Kumar et al. (1999). This observation begs the question as to whether nonlinear ENSO regime changes
65 are related to changes in the ENSO-India rainfall relationship.

66 Various mechanisms have been proposed for explaining ENSO skewness. Kang and Kug (2002) suggested
67 that the asymmetry between the magnitude of El Niño and La Niña events is related to the relative westward
68 displacement of zonal wind stress anomalies during La Niña events compared to El Niño events. Jin et al., (2003) and
69 An and Jin (2004) found that ENSO asymmetry is related to nonlinear dynamical heating (NDH), where the magnitude
70 of NDH is related to the propagation characteristics of ENSO. During strong El Niño events like the 1982/1982 and
71 1997/1998 events, SST anomalies were found to propagate eastward, with the eastward propagation tending to produce
72 more NDH compared to weak EL Niño events when NDH is minimal (An and Jin, 2004). Since the late 1970s there
73 has been a propensity for eastward propagation characteristics of ENSO (Santoso et al., 2013), contrasting with the
74 time period before the 1970s that consisted of the relatively weak El Niño events of 1957/1958 and 1972/1973 (An
75 and Jin, 2004; An, 2009). More recently, Su et al. (2010) showed that vertical temperature advection may have an
76 opposing effect on ENSO asymmetry and that the asymmetry in the extreme eastern equatorial Pacific is related to
77 meridional ocean temperature advection.

78 Previous investigators have used different metrics to quantify ENSO asymmetry. To measure the nonlinear
79 character of ENSO, An and Jin (2004) used time-domain metrics such as skewness and maximum potential intensity
80 (MPI) to quantify the skewness of SST anomalies and the skewness of individual ENSO events, respectively. An
81 (2004) applied a principal component analysis (PCA) to a 21- year moving window of tropical Pacific SST skewness
82 and found that the first PCA mode is characterized by positive skewness across the eastern equatorial Pacific and
83 negative skewness across the central equatorial Pacific. This pattern means that interdecadal changes in the
84 nonlinearity of ENSO is associated with positively skewed SST anomalies across the eastern equatorial Pacific,
85 implying that El Niño events are stronger than La Niña events. While the methods implemented in the aforementioned
86 studies provided important insights, they cannot reveal the frequency modes of ENSO that are contributing to the
87 skewness. Furthermore, the sliding-window approach is not local in the sense that it cannot quantify the strength of
88 nonlinearity at a point in time because skewness is calculated using a set of observations over some time interval.
89 While the MPI index does address the problem of quantifying the skewness of individual events, it also does not
90 provide any information regarding the frequency components contributing to ENSO skewness.

91 Recognizing the limitations of time-domain approaches, Timmermann (2003) conducted a bi-spectral
92 analysis of the Niño 3 anomaly time series, where a peak (f_1, f_2) in the bi-spectrum means there is statistical phase



93 dependence among oscillators with frequencies f_1 , f_2 , and $f_1 + f_2$. That bi-spectral analysis revealed statistically
94 significant bi-spectral power at several frequency pairs, including (0.038, 0.038), (0.028, 0.028), (0.0225, 0.0225),
95 (0.0045, 0.032), and (0.0045, 0.045) [month⁻¹]. The peaks (0.0045, 0.032), and (0.0045, 0.045) [months⁻¹] were
96 identified with the nonlinear interactions among 18-year and 2-year variability. Although the analysis provided new
97 insights, the Fourier-based analysis could not reveal how the nonlinear nature of ENSO changed with time, an
98 important property to capture given how the nonlinear characteristics of ENSO are non-stationary (Santoso et al.,
99 2013). Much like the cross-wavelet power (Maraun and Kurths, 2004) and time-domain covariance, bi-spectral power
100 is not a bounded quantity and so high bi-spectral power does not always mean strong phase dependence.

101 In this study, the deficiencies associated with the above-mentioned techniques are addressed using higher-
102 order wavelet analysis, which allows for the quantification of frequency-dependent and non-stationary nonlinearities
103 in time series (Van Milligan, 2004, Elsayad, 2006; Schulte, 2016b). More specifically, the objectives of the paper are
104 the following: 1) quantify the nonlinearity of ENSO and Indian rainfall using higher-order wavelet analysis together
105 with recently developed statistical tests; (2) Determine if different nonlinear modes of ENSO are associated with
106 distinct SST patterns; and (3) develop nonlinear wavelet coherence methods to test the hypothesis that the breakdown
107 of the ENSO-India rainfall relationship in recent decades is related to the shift of ENSO from a linear regime to a
108 nonlinear one. The paper is organized as follows: In Section 2, data used are described. Section 3 includes the
109 description of the implemented methodologies. Results are presented in Section 4 and concluding remarks are
110 provided in Section 5.

111 2. Data

112 Monthly rainfall data for 5 homogenous regions (Parthasarathy et al. 1995a) were obtained from the Indian
113 Institute of Tropical Meteorology website (<http://www.tropmet.res.in>). The five homogenous regions called the
114 Peninsula, Northwest, Northeast, Central Northeast and West Central regions were constructed based on attributes
115 such as contribution to annual rainfall amount and regional/global circulation parameters (Parthasarathy et al. 1995a;
116 Azad et al., 2010). The variability of India rainfall was also analyzed using the all-India (Parthasarathy et al. 1995b)
117 rainfall time series, which is created by averaging representative rain gauges at various locations across India (Mooley
118 and Parthasarathy, 1984). The full monsoon season (June-September) and the late monsoon (August-September)
119 season were used to identify possible within-season variations in the relationships. All 6 rainfall time series considered
120 are continuous and span the time period from 1871 to 2016. To remove the influence of the annual cycle, the time
121 series was converted into anomaly time series by subtracting the 1871-2016 long-term mean for each month from the
122 individual monthly values. The anomaly time series were subsequently standardized by dividing them by their
123 respective 1871-2016 standard deviations. Because wavelet analysis focuses on specific frequency components that
124 are not impacted by long-term time-domain trends, no detrending of the data was performed.

125 The monthly data for the Niño 1+2, Niño 3, Niño 3.4, and Niño 4 indices (available at:
126 https://www.esrl.noaa.gov/psd/gcos_wgsp/Timeseries/Data/nino34.long.data) from 1871 to 2016 were used to
127 understand how the nonlinear characteristics of SSTs vary from one ENSO region to another. The Niño 1+2 index is
128 the average SST in the region with latitudinal boundaries 0° and 10°S and longitudinal boundaries 90°W and 80°W
129 and the Niño 3 index is the average SSTs in the region with latitudinal boundaries 5°N and 5°S and longitudinal
130 boundaries 150°W and 90°W. Variations in SSTs further west were described using the Niño 3.4 and Niño 4 indices,
131 where the Niño 3.4 index is defined as the average SST in the region bounded by 5°N and 5°S and 170°W and 120°W
132 and the Niño 4 index is defined as average SSTs in the region bounded by 5°N and 5°S and 160°E and 150°W. The
133 seasonal cycle was removed from these time series in the same way as it was removed from the rainfall time series.
134 Like the rainfall data, these data were not detrended.

135 The monthly SST data from 1871-2016 were based on the Hadley Centre Global Sea Ice and Sea
136 Surface Temperature (HadISST1; Rayner et al., 2003) The data at each grid point were converted to
137 monthly anomalies in the same way as they were computed for the ENSO and All-India time series.

138 3. Methods



139 3.1 Event Decomposition

140 To quantify the time-domain skewness of individual ENSO and India rainfall events, the ENSO and rainfall
141 time series were first decomposed into individual events using the event decomposition procedure outlined by Schulte
142 and Lee (2019). That is, a time series x_1, x_2, \dots, x_N with data points located at the time points t_1, t_2, \dots, t_N was partitioned
143 into subsequences comprising adjacent data points whose values are negative in the case of negative events and whose
144 values are positive in the case of positive events. A positive event was considered to begin at t_i if $x_i > 0$ and $x_{i-1} < 0$.
145 The decay phase of a positive event beginning at x_i was then defined as the time point t_j such that $t_j \geq t_i$, $x_j > 0$, $x_{j+1} <$
146 0 , and $x_k > 0$ for all k such that $i \leq k \leq j$. Negative events were identified by switching the inequalities in the statements
147 above. After the event decompositions, the peak intensity of events was calculated, where the peak intensity of a
148 negative (positive) event was the minimum (maximum) value obtained by a data point within the event period $[t_i, t_j]$.
149 The persistence of an event was defined as the number of points composing the event and the event intensity was
150 defined as

$$151 \quad I = \sum_{i=1}^M y_i \quad (1)$$

152 where the y_i are the M data points composing the event. The duration and intensity of events were depicted using
153 event spectra (Schulte and Lee, 2019).

154 3.2 Wavelet Analysis

155 To better diagnose changes in time series statistics associated with India rainfall and ENSO, we adopted a
156 wavelet analysis. The continuous wavelet transform of a time series $X = \{x_n: n = 1, 2, \dots, N\}$ is given by

$$157 \quad W_n(s) = \sqrt{\frac{\delta t}{s}} \sum_{n'=1}^N x_{n'} \psi_0 \left[(n' - n) \frac{\delta t}{s} \right] \quad (2)$$

158 where s is wavelet scale, ψ_0 is an analyzing wavelet, δt is a time step (1 month in this study), and n is time. The
159 sample wavelet power spectrum $|W_n(s)|^2$ measures the energy content of a signal at time n and scale s . The commonly
160 used Morlet wavelet with angular frequency $\omega = 6$ was used throughout this paper because it balances time and
161 frequency localization. The reader is referred to Torrence and Compo (1998) and Grinsted et al. (2004) for details
162 about wavelet analysis.

163 Wavelet coherence was used to quantify the linear relationship between two time series as a function of
164 frequency and time. Wavelet coherence between two time series X and Y is given by

$$165 \quad R_n^2(s) = \frac{|s s^{-1} W_n^{XY}(s)|^2}{s(s^{-1} |W_n^X(s)|^2) s(s^{-1} |W_n^Y(s)|^2)}, \quad (3)$$

166 where S is a smoothing operator (Grinsted et al., 2004) and $W_n^{XY}(s)$ is the cross-wavelet power spectrum. A coherence
167 value of 1 indicates the strongest possible association between two variables at the scale s and time n . Large values of
168 wavelet coherence correspond to time points and scales for which the relative phase difference between two time
169 series varies little over a time interval. That is, two time series are perfectly coherent at the scale s if for some constant
170 c $\phi_n^X(s) - \phi_n^Y(s) = c$, where $\phi_n^X(s)$ is the phase associated with X and $\phi_n^Y(s)$ is the phase associated with Y . If the
171 relative phase relationship is sufficiently stable, then the wavelet coherence will emerge as statistically significant
172 (Section 3.4).

173 In the context of the Indian monsoon, strong coherence between rainfall and a climate pattern (e.g. ENSO)
174 at a scale s indicates shared temporal characteristics between a climate pattern and rainfall. Because theory supports a
175 causal link between ENSO and monsoon variability, strong coherence means that ENSO modulates rainfall. That is,
176 when ENSO is in a warm phase at the scale s , negative rainfall anomalies are preferred; when ENSO is in a cool phase,
177 the preference is reversed. As a result, the rainfall time series will inherit the temporal characteristics of the climate
178 forcing time series at a scale s . If the climate forcing time series is strongly periodic, then the otherwise noisy rainfall
179 time series could become periodic as well.



180 **3.3 Higher-order Wavelet Analysis**

181 Although the wavelet power spectrum is useful for quantifying the signal energy at a scale s and time n , it
 182 cannot determine if there is a nonlinear relationship among different frequency components. In fact, the power
 183 spectrum can only fully describe time series in frequency space in the case of linear systems in which the output is
 184 proportional to the input (King, 1998). For nonlinear systems, higher-order moments exist, and the frequency
 185 decomposition of higher-order moments such as skewness is necessary for a more complete description of the time
 186 series. Thus, higher-order wavelet methods were adopted to determine the frequency components contributing
 187 skewness without assuming stationarity like Fourier-based bicoherence analysis.

188 The type of nonlinearities that produce skewness are quadratic nonlinearities in which the scales s_1 , s_2 , and
 189 s_3 satisfy the sum rule

190
$$\frac{1}{s_3} = \frac{1}{s_1} + \frac{1}{s_2} \quad (4)$$

191 and the wavelet phases satisfy

192
$$\phi_n(s_3) = \phi_n(s_1) + \phi_n(s_2). \quad (5)$$

193 These types of nonlinearities arise, for example, when a sinusoid is squared, in which case a harmonic is produced.

194 In this paper, the frequency components contributing to the skewness of a times series were quantified using
 195 local and global wavelet-based auto-bicoherence methods (Schulte, 2016b). Global auto-bicoherence was computed
 196 using the equation

197
$$bi_{global}^X(s_1, s_2) = \frac{|B_{global}^X(s_1, s_2)|^2}{(\sum_{n=1}^N |W_n^X(s_1)W_n^X(s_2)|^2)(\sum_{n=1}^N |W_n^X(s_3)|^2)}, \quad (6)$$

198 where

199
$$B_{global}^X(s_1, s_2) = \sum_{n=1}^N \widehat{W}_n^X(s_3)W_n^X(s_1)W_n^X(s_2) \quad (7)$$

200 is the global bi-spectrum and the hat denotes the complex conjugate. Identical to wavelet coherence, auto-bicoherence
 201 is bounded by 0 and 1, a value of 1 indicating the strongest possible phase coupling among the phases $\phi_n(s_3)$, $\phi_n(s_2)$,
 202 and $\phi_n(s_1)$ such that sum rule Eq. (5) is satisfied. A peak in the auto-coherence spectrum at (s_1, s_2) means there is
 203 phase coupling between oscillatory modes with scales s_1 , s_2 , and s_3 . High auto-bicoherence at (s_1, s_2) can also mean
 204 that the same oscillatory modes are contributing to the skewness of the time series.

205 While the global auto-bicoherence spectrum is useful for identifying nonlinear triads, it cannot determine
 206 how the strength of phase coupling changes with time. To determine if the strength of the phase coupling changes
 207 temporally, the local auto-bicoherence spectrum (Schulte, 2016b) given by

208
$$bi_n^X(s_1, s_2) = \frac{|s s_1^{-1} B_n^X(s_1, s_2)|^2}{s(s_1^{-1} |W_n^X(s_1)W_n^X(s_2)|^2) s(s_1^{-1} |W_n^X(s_3)|^2)}, \quad (8)$$

209 was computed, where $B_n^X(s_1, s_2)$ is the local bi-spectrum given as

210
$$B_n^X(s_1, s_2) = \widehat{W}_n^X(s_3)W_n^X(s_1)W_n^X(s_2). \quad (9)$$

211 In this study, we focused on the local diagonal slices of the auto-bicoherence spectrum, which consists of all points
 212 such that $s_1 = s_2$ so that Eq. (4) implies that $s_3 = s_1/2$. In this special case, the local auto-bicoherence spectrum
 213 was calculated using the equation

214
$$bi_n^X(s_1, s_1) = \frac{|s s_1^{-1} B_{local}^X(s_1, s_1)|^2}{s(s_1^{-1} |W_n^X(s_1)W_n^X(s_1)|^2) s(s_1^{-1} |W_n^X(\frac{s_1}{2})|^2)} \quad (10)$$



215 to reveal the time-evolution of auto-bicoherence estimates located along the diagonal slice in the global spectra. Bi-
216 phase corresponding to each point in the local auto-bicoherence spectrum was used to quantify the local cycle
217 geometry of the time series. Local bi-phase is given by

$$218 \quad \psi_n(s_1, s_2) = \phi_n(s_1) + \phi_n(s_2) - \phi_n(s_3) \quad (11)$$

219 and measures the skewness and asymmetries of waveforms. A bi-phase of 0° means that the relationship among the
220 scale components produces positive skewness with respect to a horizontal axis so that positive deviations from the
221 mean are larger than negative deviations from the mean. On the other hand, a bi-phase of 180° indicates negative
222 skewness with respect to the mean. Bi-phases near -90° or 90° indicate the presence of asymmetric cycle geometry
223 (King, 1998; Maccarone, 2014; Schulte, 2016b), indicating that a time series rises (falls) more quickly than it falls
224 (arises).

225 To be consistent with the wavelet power and coherence analyses, results for the higher-order wavelet analysis
226 were casted in terms of Fourier period rather than wavelet scale. The Fourier period corresponding to s_i was denoted
227 by p_i , where the Fourier period is obtained by multiplying s_i by 1.03 for the Morlet wavelet (Torrence and Compo,
228 1998). Thus, the local diagonal slice of the auto-bicoherence spectra were plotted using the Fourier period p_1
229 corresponding to s_1 as the vertical axis and time as the horizontal axis. High (or statistically significant) local auto-
230 bicoherence at p_1 and time n means that there is phase dependence between modes with periods p_1 and $p_1/2$ at time
231 n because $2p_3 = p_1$ according to Eq. (4) when $p_1 = p_2$. In other words, the local diagonal slice determines if there is
232 phase coupling between an oscillatory mode and its harmonic at various time points.

233 3.4 Statistical Hypothesis Testing

234 The statistical significance of all wavelet spectra was evaluated using the cumulative area-wise test (Schulte,
235 2016a; Schulte, 2018) to account for the simultaneous testing of multiple hypotheses (Maraun and Kurths, 2004;
236 Maraun et al., 2014). To perform the cumulative area-wise test, the point-wise test p-values associated with all points
237 in the wavelet domain had to be estimated using theoretical red-noise backgrounds for wavelet power and Monte Carlo
238 methods for wavelet coherence and auto-bicoherence (Torrence and Compo, 1998, Grinsted et al., 2004, Schulte
239 2016b). After the point-wise test implementations, the cumulative area-wise test was used to assess the statistical
240 significance of points in the wavelet domain by tracking how the normalized area of contiguous regions of point-wise
241 significance changed as the point-wise significance level was varied. The test was applied at the 5% cumulative area-
242 wise significance level using point-wise significance levels ranging from 0.02 to 0.98 because this choice of point-
243 wise significance levels was shown to result in the cumulative area-wise test outperforming the point-wise test in
244 terms of true positive detection for high signal-to-noise ratios despite how the cumulative area-wise test is more
245 stringent. Technical details of the testing procedure can be found in Schulte (2018) and in Appendix A.

246 To assess the statistical significance of the global auto-bicoherence estimates, a modified version of the
247 cumulative area-wise test was applied. In the modified version of the cumulative area-wise test, the normalized area
248 of patches was computed by dividing patch area by the product $\hat{s}_1 \hat{s}_2$, where \hat{s}_1 is the mean first-coordinate of the patch
249 and \hat{s}_2 is the mean second coordinate. The means were calculated by assuming that the point-wise significance regions
250 are polygons with a set of vertices (Schulte et al., 2015). The reason for this modified normalized area is that dividing
251 area by say, \hat{s}_1^2 , retained the correlation between normalized area and s_2 . The test was applied using the same point-
252 wise significance levels that were used to assess the statistical significance of wavelet power and coherence.

253 To further assess statistical significance of wavelet quantities, a topological significance test (Schulte et al.
254 2015; Schulte 2018) and a cumulative arc-wise test was also applied to the wavelet spectra. The implementation of
255 the topological significance test involved the computation of the number of holes and contiguous point-wise
256 significance regions at a discrete set of point-wise significance levels, resulting in persistent homology profiles. The
257 topological significance and cumulative arc-wise tests were applied at the 5% significance level, and the point-wise
258 significance levels used ranged from 0.02 to 0.98. The critical levels of the test were estimated using Monte Carlo
259 methods by generating 1000 realizations of a red-noise process with lag-1 auto-correlation coefficients equal to that
260 of the input time series.



261 **3.5 Higher-order Coherence**

262 Although wavelet coherence spectra can provide information regarding how the relationship between two
 263 climate variables changes at a scale s , it cannot completely explain why the time-domain correlation between the
 264 climate variables temporally fluctuates. The reason is that linear wavelet coherence only examines how well the
 265 variance of one time series corresponds to the variance of another at a scale s because linear coherence is determined
 266 by the wavelet power spectra of the time series. That is, linear coherence between two climate variables means that
 267 larger fluctuations in one time series produce larger fluctuations of another climate variable at the scale s . However,
 268 for two time series to be perfectly correlated in the time domain, higher skewness of one climate variable must also
 269 correspond to higher skewness of the other climate variable.

270 Recognizing that skewness is important for better understanding time-domain correlation changes, the
 271 quantity

272
$$Bi_n^2(s) = \frac{|S_{smooth}^{-1} B_n^{XY}(s_1, s_2)|^2}{s(S_{smooth}^{-1} |B_n^X(s_1, s_2)|^2) s(S_{smooth}^{-1} |B_n^Y(s_1, s_2)|^2)}, \quad (12)$$

273 called third-order coherence (nonlinear coherence, hereafter) was used to determine if changes in the skewness of X
 274 are associated with changes in the skewness of Y (see Appendix B for a more general definition). In Eq. (12), S_{smooth}
 275 is one of the three scales, and $B_n^{XY}(s_1, s_2)$ is the third-order cross-wavelet power spectrum, which is the product of the
 276 bi-spectrum of X and the conjugate of the bi-spectrum of Y , the higher-order analog of the cross-wavelet power
 277 spectrum. The word cross-bispectrum was not used to avoid confusion with cross-bicoherence analysis (Van
 278 Milligen, 1995). Like wavelet coherence, the nonlinear coherence is bounded by 0 and 1, a value of 1 indicating that
 279 the bi-spectra of X and Y at (s_1, s_2) are perfectly and linearly correlated. The statistical significance of nonlinear
 280 coherence was assessed using Monte Carlo methods and the cumulative area-wise test in the same way as it was used
 281 to assess the statistical significance of wavelet coherence.

282 Another way to interpret higher-order wavelet coherence is using linear and nonlinear modes. A linear mode
 283 $\gamma_{s_i}^X$ is the signal component of X at the scale s_i obtained by setting all wavelet coefficients to zero except those at s_i
 284 and taking the inverse wavelet transform of the result. Because linear modes are only composed of a single frequency
 285 component, the local cross-correlation (coherence) between $\gamma_{s_i}^X$ and $\gamma_{s_i}^Y$ is only impacted by the variances of X and Y
 286 at s_i . On the other hand, nonlinear coherence measures the local cross-correlation between the skewness of $\gamma_{s_1}^X + \gamma_{s_2}^X +$
 287 $\gamma_{s_3}^X$ and $\gamma_{s_1}^Y + \gamma_{s_2}^Y + \gamma_{s_3}^Y$ or between $\gamma_{s_1}^X + \gamma_{s_{1/2}}^X$ and $\gamma_{s_1}^Y + \gamma_{s_{1/2}}^Y$ in the case that $s_1 = s_2$.

288 To better understand nonlinear coherence, we supposed that

289
$$\phi_n^X(s_1) - \phi_n^Y(s_1) = c_1 \quad (13)$$

290
$$\phi_n^X(s_2) - \phi_n^Y(s_2) = c_2 \quad (14)$$

291
$$\phi_n^X(s_3) - \phi_n^Y(s_3) = c_3 \quad (15)$$

292 for constants c_1 , c_2 , and c_3 . Adding Eqs. (13) and (14) and subtracting Eq. (15) from the result produced the equality

293
$$\phi_n^X(s_1) + \phi_n^X(s_2) - \phi_n^X(s_3) - (\phi_n^Y(s_1) + \phi_n^Y(s_2) - \phi_n^Y(s_3)) =$$

 294
$$\psi_n^X(s_1, s_2) - \psi_n^Y(s_1, s_2) = \psi_n^{bi}(s_1, s_2) = K, \quad (16)$$

295 for some constant $K = c_1 + c_2 - c_3$. Thus, if X is perfectly nonlinear coherent with Y , then X and Y must be perfectly
 296 coherent at the three scales participating in the phase coupling. Even if the coherence is perfect at two scales, the
 297 relative bi-phase $\psi_n^{bi}(s_1, s_2)$ will fluctuate randomly if the relative phase difference at the remaining scale fluctuates
 298 randomly so that the nonlinear coherence will be low. Thus, if nonlinear coherence is high, then there must be some
 299 non-random relationship between X and Y at all three scales even if high linear coherence was not identified at one or
 300 more scales. This theoretical idea suggests that nonlinear coherence can uncover relationships that linear coherence
 301 cannot (see Figure S1 in supplementary material).



302 The relative bi-phase difference $\psi_n^{bi}(s_1, s_2)$ is the higher-order analog of the relative phase difference
 303 between two time series. It measures how much the cycle geometry of one time series lags that of another. A lagged
 304 bi-phase of 180° means that the skewness or asymmetry of the forcing time series is opposite to that of the response.
 305 For example, if the forcing has positive skewness, then the response will have negative skewness. If the relative bi-
 306 phase is 0° , then negative (positive) skewness of the forcing produces negative (positive) skewness of the response,
 307 contributing to the positive time-domain correlation between the time series. Scales and time points for which
 308 nonlinear coherence is high are where the relative bi-phase is stable.

309 Throughout this paper, we will focus on nonlinear coherence computed along the diagonal slices ($p_1 = p_2$)
 310 of the time series bi-spectra. The nonlinear coherence spectra are then plotted using p_1 as the vertical axis and time as
 311 the horizontal axis. High nonlinear coherence at p_1 and n means that the skewness or asymmetry between $\gamma_{p_1}^X + \gamma_{p_1/2}^X$
 312 and $\gamma_{p_1}^Y + \gamma_{p_1/2}^Y$ are locally cross-correlated.

313 To demonstrate the concept of nonlinear coherence, we considered a simple example in which the nonlinear
 314 climate forcing time series was given by

$$315 \quad F(t) = \cos\left(\frac{2\pi}{p_1}t + \varphi\right) + \gamma(t) \cos\left(\frac{2\pi}{p_3}t + 2\varphi\right) + W_F(t) \quad (17)$$

316 and the response to the forcing was given as

$$317 \quad R(t) = \cos\left(\frac{2\pi}{p_1}t + \varphi\right) + w_R(t), \quad (18)$$

318 In Eq. (17), $\gamma(t)$ is a time-varying nonlinear coefficient, $w_F(t)$ is Gaussian white noise associated with the forcing,
 319 $w_R(t)$ is Gaussian white noise associated with the response, $\varphi = 0$ is phase, and $p_1 = 2p_3 = 32$. The nonlinear
 320 coefficient was assumed to be a linear function of time, i.e.,

$$321 \quad \gamma(t) = t/500. \quad (19)$$

322 The effect of the coefficient is to linearly increase the variance of $F(t)$ at $p_3 = 16$ and increase the strength of the
 323 quadratic phase coupling between the modes with periods $p_3 = p_1/2 = 16$ and $p_1 = 32$.

324 As shown in Figure 1a, $F(t)$ (black curve) and $R(t)$ (thick green curve) evolve coherently from $t = 0$ to $t =$
 325 200. After $t = 200$, $F(t)$ begins to noticeably exceed $R(t)$ at certain time points (e.g. $t = 430$) while the relationship
 326 between them at other points is reversed (e.g. $t = 450$) in the sense that a positive forcing produces a negative response.
 327 As a result, the correlation between $F(t)$ and $R(t)$ weakens (Figure 1b). An inspection of the wavelet coherence
 328 spectrum (Figure 2a) reveals that the coherence at $p_1 = 32$ is strong and stable so that changes in the relationship
 329 strength at that time scale is not the cause of the weakening time-domain correlation. The coherence at all other periods
 330 is also stationary by construction so that it is not the changing relationship strength at any scale that is causing the
 331 time-domain correlation weakening. However, the variance of $F(t)$ at $p_3 = 16$ increases with time (not shown) and
 332 the coherence between $F(t)$ and $R(t)$ is also weak at that time scale, implying that larger fluctuations in $F(t)$ at $p_3 = 16$
 333 are not accompanied by larger fluctuations in $R(t)$. Thus, variance increase of $F(t)$ is one reason for the weakening
 334 time-domain correlation. However, both linear coherence and wavelet power cannot explain why the skewness of $F(t)$
 335 increases, while the skewness of $R(t)$ is relatively stable (Figure 1c).

336 To further diagnose a cause of the weakening time-domain correlation, it is necessary to look at the auto-
 337 bicoherence spectrum of $F(t)$ and the nonlinear wavelet coherence spectrum. An inspection of the local auto-
 338 bicoherence spectrum of $F(t)$ (Figure 2b) reveals that the auto-bicoherence at $p_1 = 32$ is increasing with time, indicating
 339 that the phase coupling between modes with periods $p_3 = 16$ and $p_1 = 32$ is strengthening with time. The bi-phase of
 340 0° , as indicated by arrows pointing to the right, confirms that the phase coupling is contributing to the positive
 341 skewness seen in Figure 1a to an increasing degree. Furthermore, the nonlinear coherence between $R(t)$ and $F(t)$ is
 342 weak and mostly statistically insignificant at $p_3 = 32$ (Figure 2c), implying that the skewness of $F(t)$ produced from
 343 the phase coupling between the modes $p_3 = 16$ and $p_1 = 32$ does not influence the skewness of $R(t)$. In other words,
 344 the skewness of $\gamma_{16}^F + \gamma_{32}^F$ is uncorrelated with the skewness of $\gamma_{16}^R + \gamma_{32}^R$, where $\gamma_{16}^F + \gamma_{32}^F$ is the sum of the cosines
 345 in Eq. (17) and the components of $W_F(t)$ at $p_3 = 16$ and $p_1 = 32$. The nonlinear mode $\gamma_{16}^R + \gamma_{32}^R$ is the sum of the



346 cosine in Eq. (18) and the components of $w_R(t)$ at $p_3 = 16$ and $p_1 = 32$. The weak nonlinear coherence also means that
347 $\psi_n^F(32, 32) - \psi_n^R(32, 32)$ fluctuates randomly (not shown). Thus, the skewness of $R(t)$ in the time-domain is
348 practically uncorrelated with the skewness of $F(t)$ because the skewness of $F(t)$ is solely related to the phase coupling
349 between the modes with periods $p_3 = 16$ and $p_1 = 32$. Thus, the increase in skewness of $F(t)$ also contributes to the
350 weakening time-domain correlation.

351 The lack of nonlinear coherence at time scales for which $F(t)$ is nonlinear has implications for empirical
352 prediction. At time points when $F(t)$ is positively skewed $R(t)$ is overestimated because $R(t)$ is not inheriting the
353 skewness of $F(t)$. In other words, a large forcing produces an unexpectedly small response. That is, if one created a
354 linear regression model based on the relationship between $F(t)$ and $R(t)$ from $t = 0$ to $t = 200$ one would find that a
355 forcing value of, say, 1 would produce a response close to 1. If the same model was used to predict $R(t)$ at, say, $t =$
356 430 one would predict that the forcing with value around 2 should result in a response near 2. However, because the
357 relatively large value $F(430)$ results from skewness and $R(t)$ is uncorrelated with its skewness, the response is only as
358 strong as the part of $F(t)$ not resulting from the quadratic phase coupling. The more nonlinear $F(t)$ becomes, the more
359 $F(t)$ will overestimate $R(t)$ when $F(t)$ is positively skewed. Similarly, the positive forcing produces a negative response
360 at $t = 450$ because of skewness and not simply a change in variance. Nonlinear coherence allows for the quantification
361 and identification of these time-domain aberrations.

362 The weakening relationship shown in Figure 1b could lead a researcher to believe that another direct forcing
363 must be directly influencing $R(t)$. This belief could lead to the applications of partial coherence (Ng, and Chan, 2012)
364 and partial correlation analyses to identify another influential forcing mechanism. However, in this case, there are no
365 other direct forcing mechanisms; the weakening time-domain relationship is solely related to how $F(t)$ transitioned
366 from a linear process to a nonlinear process. That is, the change is related entirely to how the skewness of $F(t)$ changed.
367 However, the phenomena influencing the linearity of $F(t)$ would be at least indirectly related to $R(t)$.

368 4. Results

369 4.1 Event Decomposition of ENSO and Indian Monsoon time series

370 The time series of the Niño 1+2 and Niño 4 indices together with the corresponding event spectra are shown
371 in Figures 3 and Figures 4, where we have chosen to show the results for the Niño 4 and Niño 1+2 indices because
372 they provide contrasting results. For the Niño 1+2 time series, a few recent notably intense (Figure 3b) warm events
373 are located around 1982/1983, 1997/1998, and 2015/2016 coinciding with the strongest El Niño events in recent
374 decades (McPhaden, 1999, Hu and Fedorov, 2017; Santoso et al, 2017). The event spectra for the Niño 3 and Niño
375 3.4 indices identified notably intense warm events that occurred after the 1970s (not shown). A few notably intense
376 events were also found in the late 1800s and early 1900s, indicating that intense ENSO events are not unique to recent
377 decades.

378 To visualize how skewness changes temporally, a 20-year sliding skewness analysis was conducted. As
379 shown in Figure 5a, the skewness of the Niño 1+2 index is enhanced during the early 1880s, near zero around the
380 1930's and early 1940's, and especially enhanced after the 1970s. It also appears that there is an upward trend in
381 skewness beginning around the 1940s, where the skewness peaks around 2000. In contrast to the Niño 1+2 index, the
382 skewness of the Niño 4 index becomes more negative after the 1970s, and the magnitude of the skewness is generally
383 smaller than that of the Niño 1+2 time series. This finding suggests that the transition of the Niño 1+2 time series to a
384 nonlinear regime was more pronounced than the transition associated with the Niño 4 time series. Interestingly, a 20-
385 year sliding skewness analysis of All-India rainfall reveals that the skewness of June-September All-India rainfall
386 remains close to zero until the 1990s despite the upward trend in Niño 1+2 skewness beginning in the 1940s (Figure
387 5a). However, the skewness of June-September All-India rainfall becomes more negative in the 1990s and 2000s, but
388 it is unclear if that negative skewness is related to ENSO because the skewness of the Niño 1+2 and Niño 4 indices
389 do not change as abruptly. Negative June-September All-India rainfall skewness is accompanied by enhanced positive
390 skewness of the Niño 1+2 indices prior to the 1940s, which is consistent with how All-India rainfall is negatively
391 correlated with the Niño 1+2 index time series during that time period (Figures 5b and 5c). Our results suggest that
392 All-India rainfall skewness is more correlated with ENSO skewness prior to the 1930s than it is in recent decades.



393 **4.2 The time-domain Indian Rainfall-ENSO Relationship.**

394 Given the non-stationarities in skewness can influence the time-domain correlation between two time series
395 (Figure 1b), it is reasonable to hypothesize that the All-India rainfall relationship with the Niño 1+2 and Niño 4 indices
396 could be non-stationary given that changes in Indian rainfall skewness do not always correspond with changes in
397 ENSO skewness. To test the hypothesis, a 20-year sliding correlation analysis was conducted between these ENSO
398 indices and All-India rainfall for the full (June-September) and late monsoon (August-September) seasons. The
399 correlation between the time series of the Niño 1+2 and Niño 4 indices and All-India rainfall was computed directly
400 without seasonal averaging.

401 As shown in Figure 5b, the relationship between full season India rainfall and the Niño 1+2 index generally
402 weakens from the 1800's to the 2000s. In contrast, the Niño 4 index relationship with All-India rainfall for the full
403 season appears to have no long-term trend, resulting in the Niño 4 index becoming more strongly correlated with All-
404 India rainfall than the Niño 1+2 index after the 1970's. The relationship between Indian rainfall and time series for
405 the Niño 3 and Niño 3.4 indices was also found to be relatively weak after the 1970s (not shown).

406 The stronger relationship between All-India rainfall and the Niño 4 index compared to the Niño 1+2
407 relationship with All-India rainfall after the 1970s is more evident in the late-season analysis (Figure 5c). An abrupt
408 weakening of the Niño 1+2-rainfall relationship occurs around the 1970's, with the relationship reversing around the
409 1990s. A comparison of Figures 5a and Figures 5c reveals that the weakening and reversal of the relationship occurs
410 during the time period when the Niño 1+2 index is especially skewed, suggesting that ENSO skewness changes could
411 be contributing to changes in the time-domain correlation between ENSO and All-India rainfall. However, we have
412 not shown that ENSO skewness exceeds a red-noise background (Sections 4.2 and 4.3) so that ENSO skewness
413 changes and time-domain correlation impacts could still be noise and unpredictable. Nevertheless, this reversal is
414 consistent with how Fan et al. (2017) found that the SST composite difference between drought and drought-free El
415 Niño years during the 1979-2012 period features warming across the central equatorial Pacific and cooling across the
416 eastern equatorial Pacific, whereas the SST composite for the 1978-1987 period features warming across the eastern
417 to central equatorial Pacific. It also noted that Niño 1+2 index-rainfall relationship is also relatively weak during the
418 late 1800's when Niño 1+2 skewness is relatively high (Figure 5a).

419 A rapid weakening is also seen in the Niño 4-rainfall relationship, but it appears to begin in the 1980's, which
420 is later than the Niño 1+2-rainfall relationship breakdown. Nevertheless, the weakening Niño 4-India rainfall
421 relationship coincides with the enhanced negative skewness of the Niño 4 index (Figures 5a). The fact that Niño 1+2
422 skewness is greater than Niño 4 skewness after 1970s and that the Niño 1+2 index relationship with All-India rainfall
423 weakens more abruptly than the Niño 4 index relationship with All-India rainfall suggests that skewness could at least
424 partially explain the temporal fluctuations in the relationships seen in Figure 5. Thus, a further investigation is needed
425 to better understand the temporal changes in ENSO statistics and their impact on the ENSO-India rainfall relationship.

426 **4.3. Wavelet Power Analysis and Coherence**

427 To better understand the non-stationarity of ENSO statistics, the wavelet power spectra associated with the
428 ENSO time series were computed (Figure 6). Enhanced variance in the 16- to 64-month band is seen after 1965 for
429 all the time series. For the Niño 3 and Niño 4 time series, there is also enhanced variance in the 16- to 64-month period
430 band from 1875 to 1895, whereas the enhanced variance persists to around 1905 for the Niño 3.4 time series. Another
431 important aspect of the wavelet power spectra is that the cumulative area-wise significance regions extend across
432 many periods. For example, in the wavelet power spectrum of the Niño 1+2 index, there is a period-elongated region
433 around 1997/1998 extending from a period close to 4 months to a period around 64 months. A similar feature is also
434 evident in the wavelet power spectrum of the Niño 3 and Niño 3.4 indices but appears to be less pronounced in the
435 wavelet power spectrum of the Niño 4 index. The appearance of holes in contoured regions suggests that there are
436 oscillatory modes with nearby frequencies (Schulte, et al., 2015), though the wavelet power spectra cannot determine
437 if there is phase coupling between the oscillatory modes.

438 The wavelet coherence spectrum shown in Figure 7, indicates that the All-India rainfall relationship with the
439 Niño 1+2 and Niño 4 indices in the 16- to 64-month period band breaks down after 1995, which is consistent with the



440 findings from the sliding correlation analysis shown in Figure 5. The relationship between rainfall and these ENSO
441 indices also weakens around 1925, but this weakening does not appear in the sliding correlation analysis. Note that
442 the lack of coherence after 1995 coincides with the enhanced ENSO variance, implying that higher ENSO variance
443 need not be associated with higher All-India rainfall variance at those time scales. This result implies that intense
444 ENSO events arising from variance in the 16- to 64-month period band need not correspond with unusual monsoon
445 seasons. Indeed, the 1997/1998 ENSO event, which coincides with high power in the 16- to 64-month period band,
446 was associated with a near-normal 1997 monsoon season. More generally, these results imply that the difference Niño
447 1+2 – AIR is periodic in the 16- to 64-month period band, where AIR is All-India rainfall. The periodic property was
448 confirmed by computing the wavelet power spectrum of Niño 1+2 – AIR (supplementary Figure S2), with the
449 periodicity implying that time periods when ENSO overpredicts and underpredicts rainfall occur in regular intervals.
450 Thus, the result contradicts previous findings suggesting that the relationship between ENSO and Indian rainfall
451 fluctuates randomly (Yun and Timmermann, 2018). In other words, changes in ENSO variance could be contributing
452 to the weakening time-domain correlation. However, ENSO skewness is also enhanced during this time period (Figure
453 5a) so that weakening relationships may not be simply related to ENSO variance.

454 Averaging wavelet coherence in the 16 to 64-month period band further illustrates how the wavelet coherence
455 varies temporally (Figure 8). For example, wavelet coherence with both the ENSO indices reaches approximately 0.8
456 around 1975 before falling below 0.1 in the mid 1990s. Because the coherence plots shown in Figure 7 are similar, it
457 is difficult to diagnose why the sliding correlation curves shown in Figure 5 have different temporal structures. For
458 example, the period-averaged coherence shown in Figure 8 between rainfall and both the ENSO indices are identical
459 around 1998 yet the relationship between the Niño 1+2 and All-India rainfall is weaker than the relationship between
460 the Niño 4 index and All-India rainfall around that time (Figures 5b and 5c). Thus, a further analysis is needed to
461 extract information unrevealed by the linear wavelet power and coherence methods.

462 4.2. Global Auto-bicoherence

463 4.2.1 ENSO

464 As a first step for better understanding the All-India rainfall-ENSO correlation curves shown in Figure 5, the
465 global auto-bicoherence spectra associated with the ENSO time series were computed (Figure 9). For all four ENSO
466 metrics, statistically significant auto-bicoherence was identified, with the global auto-bicoherence spectrum of the
467 Niño 1+2 index containing the greatest number of statistically significant auto-bicoherence estimates. A few notable
468 peaks in the Niño 1+2 index auto-bicoherence spectrum are located at (148, 105), (148, 52), (62, 44), and (88, 88)
469 [months]. The auto-bicoherence peak at (88, 88) suggests that there is phase coupling between an 88-month mode (~
470 7 years) and a 44-month mode (~ 3.5 years). The auto-bicoherence spectrum of the Niño 3, Niño 3.4, and Niño 4
471 indices all contain statistically significant auto-bicoherence peaks at (31, 31), implying phase coupling between a 31-
472 month mode and a harmonic with a period of 15.5 months. For the Niño 3.4 index, there is also an on-diagonal peak
473 at (55.6, 55.6), whereas for the Niño 3 index the peak is slightly shifted and located at (62, 44). A third peak in the
474 Niño 3.4 spectrum was found at (105, 47), which could be associated with decadal-scale amplitude modulations of
475 ENSO, though the peak does not correspond to the linkage between the 18-year and 2-year variance identified by
476 Timmermann (2003). The differences among the auto-bicoherence spectra suggests that the nonlinear character of
477 SSTs varies spatially, which is consistent with prior work showing how skewness is generally highest in the eastern
478 equatorial Pacific and lowest in the central equatorial Pacific (An and Jin, 2004).

479 To confirm the spatial heterogeneity in the nonlinear characteristics of SSTs, the auto-bicoherence associated
480 with SSTs at a few select peaks (p_1 , p_2) were computed at each grid point in the domain bounded by 20°N and 20°S
481 and by 146°E and 80°W. The peaks were selected based on the auto-bicoherence spectra of the Niño 3.4 and Niño
482 1+2 indices. To select the peaks, local maxima in auto-bicoherence within the statistically significance regions shown
483 in Figure 9 were identified.

484 The spatial structure of auto-bicoherence corresponding to the peaks in the Niño 3.4 auto-bicoherence
485 spectrum are shown in Figure 10. The auto-bicoherence associated with the pair (31, 31) is greatest across the central
486 equatorial Pacific, with the overall spatial pattern being reminiscent of a central Pacific El Niño (Lee and McPhaden,
487 2010). This result suggests that the phase coupling between the 31-month mode and the 15.5-month mode could be



488 related to the occurrence of central Pacific El Niño events (Section 5). In contrast, the auto-bicoherence pattern
489 associated with the pair (56, 56) is more uniform, with auto-bicoherence slightly greater across the extreme eastern
490 equatorial Pacific than the central equatorial Pacific. This pattern is reminiscent of an eastern Pacific El Niño. Like
491 the pattern corresponding to the pair (31, 31), the auto-bicoherence for the pair (105, 57) tends to be greater across the
492 central equatorial Pacific. Our findings suggest that different nonlinear modes contribute to different ENSO flavors.
493 Although An and Jin (2004) and Burgers and Stephenson (1999) showed that skewness is greatest across the eastern
494 equatorial Pacific, we determined that such a time-domain approach is unable to capture frequency-dependent patterns
495 in nonlinearity.

496 The spatial auto-bicoherence plots associated with the peaks in the Niño 1+2 auto-bicoherence spectrum are
497 shown in Figure 11. The auto-bicoherence associated with the pairs (148, 53) and (148, 105) is strong across the
498 eastern equatorial Pacific but weak across the central equatorial Pacific, suggesting that the phase coupling between
499 the 148- and 105-month modes and between the 148- and 53-month modes are associated with the skewness of eastern
500 equatorial Pacific SSTs. The pattern associated with the pair (62, 44) is reminiscent of an eastern Pacific El Niño and
501 the auto-bicoherence associated with the pair (88, 88) is relatively weak across the entire equatorial Pacific. A
502 comparison of Figures 10 and 11 shows that there is a tendency for auto-bicoherence to be greater across the eastern
503 equatorial Pacific than the central equatorial Pacific, which is consistent with the results of An and Jin (2004) and
504 Burgers and Stephenson (1999) who found that SSTs across eastern equatorial Pacific are most skewed. The results
505 are also in agreement with Figure 5a, which shows how the magnitude of Niño 1+2 skewness is greater than that of
506 the Niño 4 skewness after the 1970s.

507 4.2.2 India Rainfall

508 The global auto-bicoherence spectra for the rainfall time series are shown in Figure 12. For all the rainfall
509 time series except for the central Northeast time series, statistically significant auto-bicoherence was identified. The
510 auto-bicoherence spectrum of the All-India time series contains four on-diagonal peaks, one located around (4,4),
511 another located at (18, 18), and two more located around (40, 40) and (90, 90) [months]. Each of these peaks indicate
512 time series components with periods 4, 18, 40, 90 months are phase coupled to the corresponding harmonics with
513 periods of 2, 9, 20, and 45 months. Such phase coupling is inconsistent with the null hypothesis of red noise, which
514 agrees with the findings of Schulte (2019) who found robust evidence that there are features embedded in the India
515 rainfall time series that exceed a red-noise background. Thus, it is natural to ask if these peaks are inherited from a
516 nonlinear climate forcing. For example, the peak (90, 90) in the All-India rainfall auto-bicoherence spectrum
517 corresponds well with the peak found in the auto-bicoherence spectra of the Niño 1+2 time series (Figure 9).

518 Figure 12 also reveals how the nonlinear characteristics corresponding to each region differ. The statistically
519 significant auto-bicoherence for the Peninsula, Northwest, West Central, and Northeast time series is mainly located
520 in regions for which p_1 and p_2 are less than 16 months. However, a peak at (256, 32) was found in the auto-bicoherence
521 spectrum of the Northeast time series, suggesting that the time series components with periods 28, 32, and 256 are
522 phase dependent. Many other differences are also seen through an inspection of Figure 12. Our findings suggest that
523 the processes governing precipitation variability in each of the regions differ (Roy and Tedeschi, 2016).

524 4.3 Local auto-bicoherence

525 4.3.1 ENSO

526 To determine if the strength of the identified nonlinearities changes with time, the local diagonal slices
527 corresponding to the global auto-bicoherence spectra shown in Figure 9 were computed. The results shown in Figure
528 13 reveal that the auto-bicoherence spectra of all ENSO time series contain statistically significant local auto-
529 bicoherence, but the spectrum of the Niño 4 index is only associated with a few statistically significant regions such
530 as the one around 2015 at a period of 32 months.

531 For the Niño 3 and Niño 3.4 time series, two features of interest are seen in the time period extending from
532 1973 to 2017 in the 16- to 64-month period band. The first feature is the time-elongated region of statistical
533 significance extending from 1973 to 2016 around a period of 61 months. This result implies that after 1973 the



534 nonlinear phase coupling between modes with periods of approximately 30.5 and 61 intensifies. This intensification
535 is consistent with studies showing that ENSO underwent a regime shift in the 1970s in which ENSO began to evolve
536 more nonlinearly than in previous decades (Santoso et al., 2013). This intensification is also evident in the Niño 1+2
537 auto-bicoherence spectrum, though the exact periods associated with the phase-coupled oscillatory modes are more
538 difficult to discern. Nevertheless, a comparison of Figures 5a and 13 reveals that enhanced skewness coincides with
539 stronger auto-bicoherence in the 32- to 64-month period, suggesting that the skewness partially arose from the stronger
540 phase coupling among modes with periods ranging from 32 to 64 months. The correspondence between auto-
541 bicoherence and time-domain skewness also holds for the Niño 3 and Niño 3.4 time series (not shown). Our findings
542 suggest that phase coupling among modes embedded in the 32- to 64-month period band plays an important role in
543 generating the skewness of ENSO warm events.

544 The second feature of interest in Niño 3 and Niño 3.4 auto-bicoherence spectra is the one that emerges around
545 1995 at a period of 31 months. Despite how recent studies indicate that the ENSO regime shift occurred around 1973,
546 this result suggests that the onset of this phase coupling occurred well after the 1970s regime shift just before the
547 1997/1998 El Niño event. Thus, the nonlinear character of, say, the 1982/1983 El Niño is different from that of both
548 the 1997/1998 and 2015/2016 El Niño events because of the additional phase coupling between the 15.5- and 31-
549 month modes. It is also noted that Figure 13 also shows that there are other time periods when ENSO behaved
550 nonlinearly, and so the recent nonlinear events may not be unique to recent decades. For example, the auto-bicoherence
551 spectrum of the Niño 3.4 time series is associated with enhanced auto-bicoherence around 1875 in the 32- to 128-
552 month period band. Nevertheless, our findings reveal that the stationarity of the phase coupling in recent decades is
553 unprecedented with respect to any other time period.

554 To confirm that the nonlinear phase coupling identified in Figure 13 is associated with skewed waveforms,
555 we inspected the corresponding local bi-phase spectra (not shown). It was found that the bi-phase in the 42- to 64-
556 month period band is generally 0° so that the nonlinear phase coupling in that period band contributes to the positive
557 skewness of the 1982/1983, 1997/1998, and 2015/2016 events.

558 The temporal change in the auto-bicoherence associated with the Niño 1+2 and Niño 4 indices was further
559 illustrated by averaging the local auto-bicoherence in the 32- to 64-month period band. As shown in Figure 8, the
560 auto-bicoherence associated with both ENSO indices increases after the 1970s. This increase in auto-bicoherence
561 coincides with the increase in skewness shown in Figure 5. Thus, the skewness of the Niño 1+2 and Niño 4 indices
562 appears to be related to the auto-bicoherence in the 32- to 64-month period band. It also noted that the auto-bicoherence
563 associated with the Niño 1+2 index peaks around 1998, which is consistent with how the 1997/1998 Niño 1+2 warm
564 event arose from nonlinear processes (An, and Jin, 2004). The auto-bicoherence was also high around the nonlinear
565 event 1982/1983 event (An and Jin, 2004), further supporting the idea that the skewness of individual Niño 1+2 warm
566 events is connected to the nonlinear phase coupling in the 32- to 64-month period band.

567 **4.3.2 Local Bicoherence of India Rainfall and Non-linear Coherence**

568 The local auto-bicoherence spectra of the India rainfall time series are shown in Figure 14. The statistically
569 significant auto-bicoherence was identified for all six time series, mainly for periods less than 64 months. The results
570 suggest that the phase coupling is many among higher frequency modes. However, for the All-India rainfall time
571 series, the auto-bicoherence spectrum reveals two time periods of statistically significant auto-bicoherence in the 64-
572 to 128-month period band. The first region extends from 1885 to 1925 and the second region extends from 1945 to
573 around 1985. The nonlinearities found in the India rainfall auto-bicoherence spectra were also found to be cumulative
574 arc-wise significant, though some differences in the results were found (Figure S3 in supplementary material). The
575 statistical significance of the results was further checked using the topological significance test (Schulte, 2019), which
576 also provided evidence that the time series are nonlinear (Figure S4 supplementary material).

577 To determine if the nonlinearities identified for All-India rainfall is related to ENSO, nonlinear coherence
578 was computed along the local diagonal slices of the auto-bicoherence spectra for both All-India rainfall and the four
579 ENSO metrics considered in this study. Furthermore, All-India rainfall is generally more strongly coherent with ENSO
580 than rainfall associated with the individual rainfall regions (Schulte, 2019) so only the results for All-India rainfall are
581 shown for brevity.



582 The results shown in Figure 15 indicate that the nonlinear wavelet coherence between All-India rainfall and
583 the time series for the all four ENSO indices is statistically significant in the 32- to 64-month period band. The
584 nonlinear coherence in this period band appears to peak around the 1972/1973 El Niño event, indicating that an
585 increase in positive skewness of ENSO should tend to coincide with enhanced negative skewness of All-India rainfall
586 around this time. As shown in Figure 8, the nonlinear coherence averaged in the 32- to 64-month period band fluctuates
587 less than linear coherence and reaches a clear global maximum around 1972/1973 before rapidly declining to a global
588 minimum around the 1997/1998 El Niño event when the Niño 1+2 index is very nonlinear (Figures 8 and 13).
589 Therefore, according to the discussion in Section 3.5, changes in ENSO skewness contributed to the weakening
590 relationships between ENSO and All-India rainfall shown in Figures 5a and 5b.

591 5. Discussion/Conclusion

592 The nonlinear nature of both ENSO and Indian rainfall were examined using higher-order wavelet methods.
593 The auto-bicoherence spectra of the four ENSO time series revealed that ENSO skewness arose from the phase
594 coupling of modes with various periods. The Niño 3.4 time series was found to contain coupling between modes with
595 period 31 and 15.5 in addition to coupling between modes with period of 61 months and 30.5 months. The phase-
596 coupling between the 31 and 15.5 modes was found to be especially strong after 1995, whereas the phase coupling
597 between the 61- and 30.5-month modes was found to intensify after the 1970s. The stronger phase coupling after the
598 1970s is consistent with how ENSO underwent a regime shift in the 1970s (Santoso et al., 2013), which was marked
599 by an increase in ENSO skewness.

600 The evolution of SSTs across the Niño 4, Niño 3.4, Niño 3, and Niño 1+2 regions was found to be nonlinear,
601 but the degree to which the time series are nonlinear are different. Overall, the Niño 1+2 time series was found to be
602 the most nonlinear, while the Niño 4 index was found to be the most linear. The spatial patterns associated with the
603 nonlinearities depend on the frequency components contributing to the nonlinearities. For example, phase coupling
604 between the modes with periods of 31 and 15.5 months was found to be strongest in the central equatorial Pacific and
605 weakest across the eastern equatorial Pacific. This finding suggest that the occurrence of central Pacific El Niño events
606 could be linked to this phase coupling, which is relevant to understanding the Indian monsoon because central Pacific
607 El Niño events have been shown to be more effective at creating drought-inducing subsidence over India (Kumar et
608 al., 2006).

609 The results from the present and previous studies (Fan et al. 2017) supports the idea that changes in the
610 ENSO-India rainfall relationship are related to ENSO flavors because ENSO nonlinearity appears to be related to
611 ENSO flavors (Figures 10 and 11), opposing the findings of other work showing that the changes are related to
612 sampling variability or to noise. According to Yun and Timmermann (2018), the changes in the time-domain
613 correlation between All-India summer rainfall (ISMR) and ENSO is consistent with the assumption that ISMR is the
614 sum of the ENSO signal and Gaussian white noise (i.e., $ISMR = ENSO + \text{white noise}$). However, for this hypothesis
615 to hold, the difference $ISMR - ENSO$ must be Gaussian white noise. As shown in this study, the nonlinear wavelet
616 coherence between ENSO metrics and All-India rainfall is weak, which means that the difference $ISMR - ENSO$ will
617 have non-Gaussian noise features so that ISMR is not consistent with a stochastically perturbed ENSO signal. The
618 retention of non-Gaussian noise features is certainly the case for $R(t) - F(t)$ in the example in Section 3.5 because the
619 difference would retain the cosine function with a period of 16. In the case of ISMR, the lack of nonlinear coherence
620 results in periodic behavior of $ISMR - ISMR$, which means that Indian rainfall is not simply a stochastically perturbed
621 ENSO signal, as noise does not contain periodicities. In contrast, if ISMR and ENSO were highly nonlinear wavelet
622 coherent, then they would have the same frequency components contributing to skewness and the difference of the
623 two would remove the skewness. Although our results cannot preclude noise as a contributor to fluctuations in the
624 time-domain correlation, the periodic nature of $ISMR - ISMR$ does suggest that monsoon forecast error for a forecast
625 based on ENSO may be predictable to some extent.

626 The fact that nonlinear coherence between rainfall and ENSO is determined by linear coherence between
627 ENSO and rainfall at two or three frequencies means that the changing time-domain correlation could be more fully
628 understood by determining why linear coherence changes at the frequencies that contribute to ENSO skewness. Such
629 an analysis could provide a more mechanistic perspective than the theoretical perspective adopted in this study. A
630 preliminary analysis showed that enhanced linear coherence between the North Atlantic Oscillation index and All-



631 India rainfall after 1995 in the 16- to 64-month period band associated with ENSO nonlinearity. This result suggests
632 that conditions across the North Atlantic (Kakade, 2000, Bhatla, 2016) could influence the nonlinear coherence
633 between ENSO and All-India rainfall and thus the corresponding time-domain correlation.

634 The higher-order wavelet analysis conducted in this study also revealed that the nonlinear nature of the
635 rainfall time series for the regions considered varied. Our results are consistent with the findings from previous work
636 showing how the physical mechanisms governing precipitation variability are different (Roy and Tedisch, 2016).
637 However, the higher-order wavelet analysis conducted in this study allowed us to determine the time scales on which
638 the rainfall times series features differ. Further research is needed to fully understand why the nonlinear characteristics
639 differ from one region to another. Future work could include conducting nonlinear coherence analyses between indices
640 of various climate modes and the rainfall times series for each region individually.

641 A few other possible physical mechanisms behind the nonlinearity of the rainfall time series were examined.
642 For example, we computed the auto-bicoherence spectrum of the IOD and sunspot time series because they have been
643 postulated as climate drivers of Indian Rainfall (Ashok et al., 2001; Ashok et al., 2004; van Loon and Meehl, 2012).
644 Although these time series were found to be highly nonlinear, the auto-bicoherence spectra of them did not correspond
645 well with the rainfall time series. We found that the IOD contains strong coupling between the modes with periods of
646 256 and 128 months and between modes with periods of 128 months and 64 months (Figures S5 and S6 in
647 supplementary material), but no such coupling was found for any of the rainfall time series. Similarly, the sunspot
648 cycle time series was associated with strong coupling between 128 -and 256-month modes (Figures S7 and S8 in
649 supplementary material) but again no such coupling was identified in the rainfall time series. Future work could thus
650 include better understanding the physical mechanisms underlying the nonlinearities identified in this study.

651 The tools used and developed in this study may have important applications in understanding how forecasting
652 systems replicate Indian rainfall and its associated teleconnections. These methods, for example, could determine if
653 forecasting systems can reproduce nonlinear characteristics of climate time series. These identifications could provide
654 new directions for improving current forecasting systems and ultimately predictions of Indian rainfall.

655

656



657

658 **Appendix A**

659 The first step (STEP 1) in assessing the cumulative-area significance of a point was the calculation of the N
 660 = 12 sets

661
$$P_{pw}^i = \{(b, a): \rho_{pw}(b, a) < \alpha_i\}, \quad (A1)$$

662 where each set is the subset of the wavelet domain consisting of points whose wavelet quantities are point-wise
 663 statistically significant at the α_i significance level. In this paper, $\alpha_1 = 0.02$, $\alpha_{12} = 0.18$, and $\alpha_{i+1} - \alpha_i = 0.02$. In the
 664 second step (STEP 2), a geometric pathway about x was computed, where a geometric pathway is a nested sequence

665
$$P_1^x \subseteq P_2^x \subseteq \dots \subseteq P_N^x \quad (A2)$$

666 such that the

667
$$P_i^x = \{(b, a): (b, a) \in P_{pw}^i, (b, a) \sim x\} \quad (A3)$$

668 are path-components of P_{pw}^i containing x . The equivalence relation \sim on P_{pw}^i makes two points in P_{pw}^i equivalent if
 669 they can be connected by a continuous path in P_{pw}^i . The third step (STEP 3) involved the calculation of the normalized
 670 area corresponding to P_i^x . The normalized area is defined as patch area divided by the square of mean scale coordinate
 671 of the patch, where A_i^x was assumed to be 0 if $P_{pw}^i = \emptyset$ or $P_{pw}^i = \{x\}$. The critical area A_i^{crit} was obtained by computing
 672 the $(1 - \alpha_c)$ th percentile of the null distribution of normalized areas corresponding to the significance level α_i , where
 673 α_c is the significance level of the cumulative area-wise test. The null distributions were constructed by generating
 674 1000 patches at the α_i significance level under the null hypothesis of red noise. More specifically, realizations of a
 675 red-noise process with lag-1 autocorrelation coefficients equal to that of input time series were used to create the
 676 wavelet spectra from which the 1000 patches were obtained. The length of the realizations was set to 200, though the
 677 length is irrelevant because patch area is not related to time series length but to the reproducing kernel of the analyzing
 678 wavelet (Schulte 2019). The final step (Step 4) was to compute

679
$$r^x = \frac{1}{N} \sum_{j=1}^N \lambda_j^x, \quad (A4)$$

680 where $\lambda_j^x = 2$ if $P_j^x / A_j^{crit} > 1$, $\lambda_j^x = 0$ if $P_j^x / A_j^{crit} < -1$, and A_j^{crit} is the critical area associated with α_j . The wavelet
 681 quantity at the point x was deemed statistically significant at the α_c cumulative area-wise level if $r^x > 1$.

682



683 **Appendix B**

684 For $p > 1$, the $(p+1)$ -th order poly spectrum of a time series X is given by

685
$$B_n^X(s_1, s_2, \dots, s_p) = \widehat{W}_n^X(s_{p+1}) \left(\prod_{k=1}^p W_n^X(s_k) \right) \quad (\text{B1})$$

686 where

687
$$\frac{1}{s_{p+1}} = \sum_{k=1}^p \frac{1}{s_k} \quad (\text{B2})$$

688 The third-order poly spectrum is the bi-spectrum, and the fourth-order poly spectrum is the tri-spectrum (Collis et al.,
 689 1998), which identifies the frequency components contributing to kurtosis. The $(p+1)$ -th order coherence between two
 690 time series is given as

691
$$R_n^2(s) = \frac{|s_{smooth}^{-1} B_n^{XY}(s_1, s_2, \dots, s_p)|^2}{s(s_{smooth}^{-1} |B_n^X(s_1, s_2, \dots, s_p)|^2) s(s_{smooth}^{-1} |B_n^Y(s_1, s_2, \dots, s_p)|^2)}, \quad (\text{B3})$$

692 where $B_n^{XY}(s_1, s_2, \dots, s_p)$ is the $(p+1)$ -th-order cross-spectrum given by

693
$$B_n^{XY}(s_1, s_2, \dots, s_p) = B_n^X(s_1, s_2, \dots, s_p) \widehat{B}_n^Y(s_1, s_2, \dots, s_p). \quad (\text{B4})$$

694 When $p = 2$, Eq. (B3), measures the local cross-correlation between skewness, and when $p = 3$ the equation
 695 measures the local cross-correlation between kurtosis.

696

697

698

699



700 References

- 701 An, S.-I., and Jin, F.-F.: Nonlinearity and asymmetry of ENSO. *J. Climate*, 17, 2399–2412, 2004.
- 702 An, S.-I., Ham, Y. G., Kug, J. S., Jin, F.-F. and Kang, I.: El Niño-La Niña asymmetry in the coupled model
703 intercomparison project simulations, *J. Climate*, 18, 2617–2627, 2005.
- 704 An S.-I.: Interdecadal changes in the El Niño-La Niña symmetry, *Geophys Res. Lett.*, 31, L23210,
705 doi:10.1029/2004GL021699, 2004.
- 706 An, S.-I.: A review of interdecadal changes in the nonlinearity of the El Niño–Southern Oscillation, *Theor. Appl.*
707 *Climatol.*, 97, 29–40, 2009.
- 708 Ashok, K., Guan, Z., Yamagata, T.: Impact on the Indian Ocean dipole on the relationship between the Indian monsoon
709 rainfall and ENSO, *Geophys Res. Lett.*, 28, 4499–4502, 2001.
- 710 Ashok K, Guan Z, Saji NH, Yamagata T (2004) Individual and combined influences of ENSO and the Indian Ocean
711 dipole on the Indian summer monsoon. *J Clim* 17:3141–3155
- 712 Bhatla, R., Singh, A. K., Mandal, B., Ghosh, S., Pandey, S. N., Abhijit, S.: Influence of North Atlantic Oscillation on
713 Indian Summer Monsoon Rainfall in Relation to Quasi-Binneal Oscillation, *Pure and Applied Geophysics*, 173, 2959–
714 2970, 2016.
- 715 Blanford, H. F.: On the connexion of the Himalaya snowfall with dry wind and seasons of drought in India, *Proc R*
716 *Soc Lond.*, 37, 3–22, 1884.
- 717 Burgers, G., Stephenson, D. B.: The ‘Normality’ of ENSO, *Geophys Res. Lett.*, 26, 1027–1030, 1999.
- 718 Cash, B.A., Barimalala, R., Kinter, J. L., Altshuler, E. L., Fennessy, M. J., Manganello, J.V., Molteni, F., Towers, P.,
719 Vitart, F.: Sampling variability and the changing ENSO–monsoon relationship, *Clim. Dyn.*, 48, 4071–4079, 2017.
- 720 Chen, W., Dong, B., and Lu, R.: Impact of the Atlantic Ocean on the multidecadal fluctuation of El Niño–Southern
721 Oscillation–South Asian monsoon relationship in a Coupled General Circulation Model, *Journal of Geophysical*
722 *Research*, 115, D17109, <https://doi.org/10.1029/2009JD013596>, 2010.
- 723 Collis, W. B., White, P. R., and Hammond, J. K.: Higher-order Spectra: The Bispectrum and Trispectrum, *Mech. Syst.*
724 *Signal Pr.*, 12, 375–394, 1998.
- 725 Duan, W., Huang, C., Xu, H.: Nonlinearity modulating intensities and spatial structures of central Pacific and eastern
726 Pacific El Niño events, *Adv Atmos Sci.*, 34, 737–756, 2017.
- 727 DelSole, T., and Shukla, J.: Climate models produce skillful predictions of Indian summer monsoon rainfall, *Geophys*
728 *Res. Lett.*, 39, L09703. <https://doi.org/10.1029/2012GL051279>, 2012.
- 729 Elsayed, M. A. K.: Wavelet Bicoherence Analysis of Wind–wave Interaction, *Ocean Eng.*, 33, 458–470, 2006.
- 730 Fan, F., Dong, X., Fang, X., Xue, F., Zheng, F., and Zhu, J.: Revisiting the relationship between the south Asian
731 summer monsoon drought and El Niño warming pattern, *Atmospheric Sci. Lett.*, 18, 175–182, 2017
- 732 Gershunov, A., Schneider, N., and Barnett, T.: Low-frequency modulation of the ENSO–Indian monsoon rainfall
733 relationship: Signal or noise?, *J. Climate*, 14, 2486–2492, 2001.
- 734 Grinsted, A., Moore, J. C., and Jevrejeva, S.: Application of the Cross Wavelet Transform and Wavelet Coherence to
735 Geophysical Time Series, *Nonlinear Proc. Geoph.*, 11, 561–566, 2004.
- 736 Hu, S and Fedorov, A. V.: The extreme El Niño of 2015–2016 and the end of global warming hiatus, *Geophys. Res.*
737 *Lett.*, 44, 3816–24, 2017



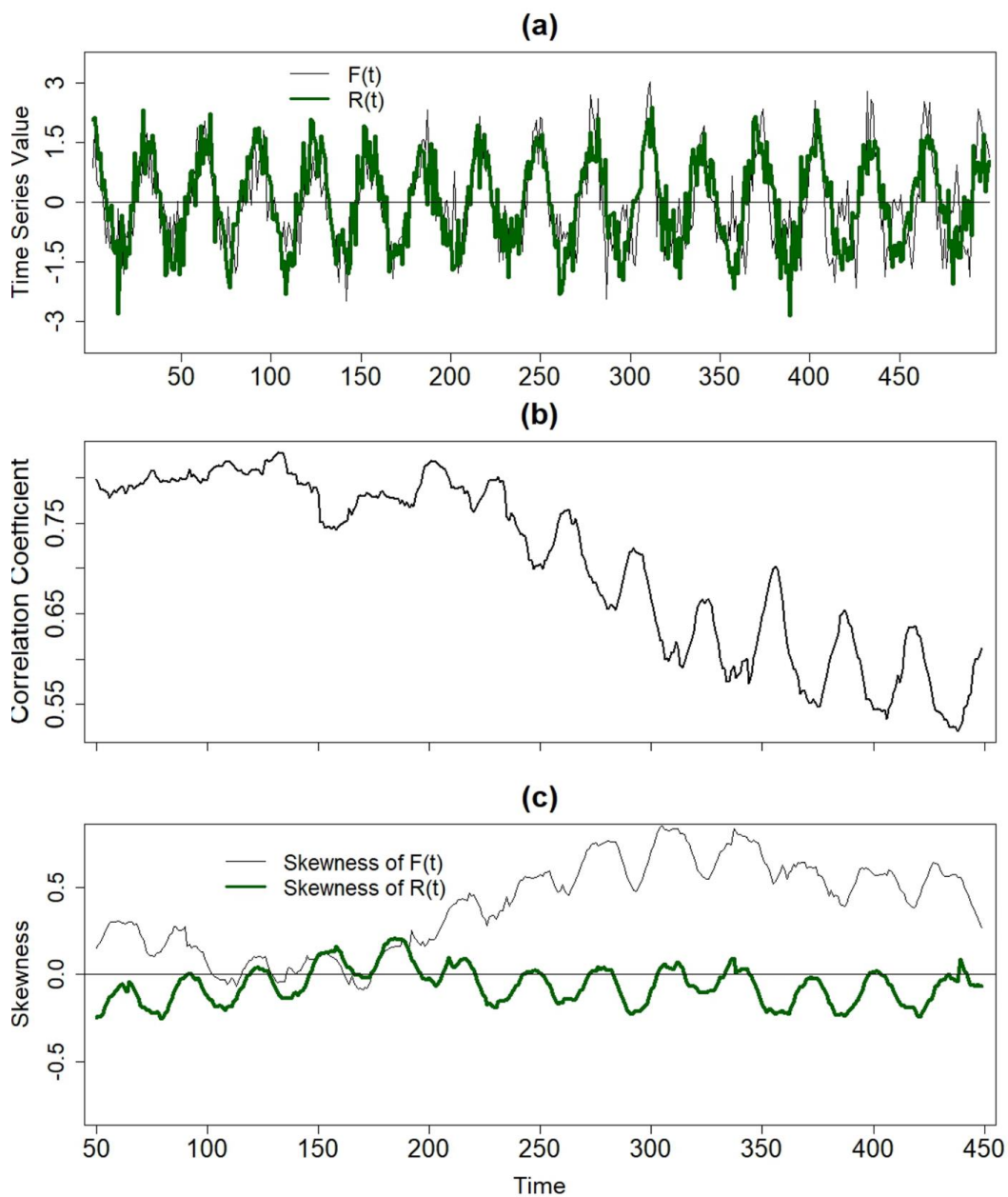
- 738 Jin, F.-F., An, S.-I., Timmermann, A., and Zhao, J.: Strong El Niño events and nonlinear dynamical heating, *Geophys. Res. Lett.*, 30, 1120, doi:10.1029/2002GL016356, 2003.
- 740 Johnson, N.C.: How Many ENSO Flavors Can We Distinguish?, *J. Climate*, 26, 4816–4827, 2013.
- 741 Johnson N. C., and Kosaka, Y.: The role of eastern equatorial Pacific convection on the diversity of boreal winter El Niño teleconnection patterns, *Clim. Dyn.*, 47, 3737–3765, 2016.
- 743 Kakade, S. B., and Dugam, S. S.: The simultaneous effect of NAO and SO on the monsoon activity over India, *Geophys Res Lett.*, 27, 3501–3504, 2000.
- 745 Kalnay, E., and Dalcher, A.: Forecasting forecast skill., *Mon. Wea. Rev.*, 115, 349–356, 1987.
- 746 Kang, I.-S., and Kug, J.-S.: El Niño and La Niña ~ sea surface ~ temperature anomalies: Asymmetry characteristics associated with their wind stress anomalies, *J. Geophys. Res.*, 107, 4372, doi:10.1029/2001JD000393, 2002.
- 748 Kestin, T. A., Karoly, D. J., Yano, J.-I., and N. A. Rayner.: Time– frequency variability of ENSO and stochastic simulations, *J. Climate*, 11, 2258–2272, 1998.
- 750 King, T.: Quantifying Nonlinearity and Geometry in Time Series of Climate, *Quaternary Sci. Rev.*, 15, 247–266, 1996.
- 752 Kucharski, F., Bracco, A., Yoo, J. H., and Molteni, F.: Low-frequency variability of the Indian monsoon–ENSO relationship and the tropical Atlantic: The “weakening” of the 1980s and 1990s, *J. Clim.*, 20, 4255–4266, 2007.
- 754 Kucharski, F., Bracco, A., Yoo, J. H., Tompkins, A. M., Feudale, L., Ruti, P., and Dell’Aquila, A.: A Gill–Matsuno-type mechanism explains the tropical Atlantic influence on African and Indian monsoon rainfall, *Quarterly Journal of the Royal Meteorological Society*, 135, 569–579, 2009.
- 757 Krishnamurthy, V., and Goswami, B. N.: Indian monsoon–ENSO relationship on interdecadal timescale, *J. Climate*, 13, 579–595, 2000.
- 759 Kripalani, R. H., and Kulkarni, A.: Climatic impact of El Niño/ La Niña on the Indian monsoon: A new perspective, *Weather*, 52, 39–46, 1997.
- 761 Kumar, K. K., Rajagopalan, B., and Cane, M. A.: On the weakening relationship between the Indian monsoon and ENSO. *Science*, 284, 2156–2159, 1999.
- 763 Kumar, K. K., Rajagopalan, B., Hoerling, M., Bates, G., Cane, M. A.: Unraveling the Mystery of Indian Monsoon Failure During El Niño, *Science*, 314, 115–119, 2006.
- 765 Lee, T., and McPhaden, M. J.: Increasing intensity of El Niño in the central-equatorial Pacific, *Geophys. Res. Lett.*, 37, L14603. DOI: 10.1029/2010GL044007, 2010.
- 767 Lu, R., Dong, B., and Ding, H.: Impact of the Atlantic Multidecadal Oscillation on the Asian summer monsoon, *Geophys. Res. Lett.*, 33, L24701. <https://doi.org/10.1029/2006GL027655>, 2006.
- 769 McPhaden, M. J.: Genesis and evolution of the 1997–98 El Niño., *Science*, 283, 950–954, 1999.
- 770 Maccarone, T. J.: The Biphase Explained: Understanding the Asymmetries in Coupled Fourier Components of Astronomical Timeseries, *Mon. Not. R. Astron. Soc.*, 435, 3547, doi:10.1093/mnras/stu1824, 2013.
- 772 Maraun, D., and Kurths, J.: Cross wavelet analysis: significance testing and pitfalls. *Nonlinear Process. Geophys.*, 11, 505–514., 2004.
- 774 Maraun, D., Kurths, J., and Holschneider, M.: Nonstationary Gaussian Processes in the Wavelet Domain: Synthesis, Estimation, and Significance Testing, *Phys. Rev. E*, 75, 016707, doi:10.1103/PhysRevE.75.016707, 2007.



- 776 Ng, E. K. W. and Chan, J. C. L.: Geophysical applications of partial wavelet coherence and multiple wavelet coherence,
777 *J. Atmos. Ocean. Tech.*, 29, 1845–1853, 2012.
- 778 Parthasarathy, B., Munot, A. A., and Kothawale, D. R.: All-India monthly and seasonal rainfall series: 1871–1993,
779 *Theoretical and Applied Climatology*, 49, 217–224, 1994.
- 780 Rayner, N. A., Parker, D. E., Horton, E. B., Folland, C. K., Alexander, L. V., Rowell, D. P., Kent, E. C., and Kaplan,
781 A.: Global analyses of sea surface temperature, sea ice, and night marine air temperature since the late nineteenth
782 century, *J. Geophys. Res.*, 108, 4407, doi: 10.1029/2002JD002670, 2003.
- 783 Roy, I. and Tedeschi, R. G.: Influence of ENSO on regional indian summer monsoon precipitation—local atmospheric
784 influences or remote influence from pacific, *Atmosphere* 7, 25, 2016.
- 785 Santoso, A., McGregor, S., Jin, F.-F., Cai, W., England, M. H., An, S.-I., McPhaden, M. J., and Guilyardi, E.: Late-
786 twentieth-century emergence of the El Niño propagation asymmetry and future projections., *Nature*, 504, 126–130,
787 2013.
- 788 Santoso, A., McPhaden, M. J., Cai, W.: The defining characteristics of ENSO extremes and the strong 2015/2016 El
789 Niño, *Rev. Geophys.*, 55, 1079–1129, 2017.
- 790 Schulte, J. A.: Statistical hypothesis testing in wavelet analysis: theoretical developments and applications to Indian
791 rainfall, *Nonlin. Processes Geophys.*, 26, 91–108, <https://doi.org/10.5194/npg-26-91-2019>, 2019.
- 792 Schulte, J. A.: Cumulative areawise testing in wavelet analysis and its application to geophysical time-series, *Nonlin.*
793 *Processes Geophys.*, 23, 45–57, 2016.
- 794 Schulte, J. A.: Wavelet analysis for non-stationary, nonlinear time series, *Nonlin. Processes Geophys.*, 23, 257–267,
795 <https://doi.org/10.5194/npg-23-257-2016>, 2016.
- 796 Schulte, J. A., Duffy, C., and Najjar, R. G.: Geometric and Topological Approaches to Significance Testing in Wavelet
797 Analysis, *Nonlin. Processes Geophys.*, 22, 139–156, 2015.
- 798 Shen, X., and Kimoto, M.: Influence of El Niño on the 1997 Indian summer monsoon, *J. Meteor. Soc. Japan*, 77,
799 1023–1037, 1999.
- 800
- 801 Slingo, J. M., and Annamalai, H.: 1997: The El Niño of the century and the response of the Indian summer monsoon,
802 *Mon. Wea. Rev.*, 128, 1778–1797, 2000.
- 803
- 804 Timmermann, A.: Decadal ENSO amplitude modulations: A nonlinear mechanism, *Global Planet. Change*, 37, 135–
805 156, 2003.
- 806 Torrence, C., and Webster, P. J.: Interdecadal changes in the ENSO-monsoon system. *J. Climate*, 12, 2679–2690.
807 1999.
- 808 van Loon, H., and Meehl, G. A.: The Indian summer monsoon during peaks in the 11 year sunspot cycle, *Geophys.*
809 *Res. Lett.*, 39, L13701, doi:10.1029/2012GL051977, 2012.
- 810
- 811 Van Milligen, B. P., Sánchez, E., Estrada, T., Hidalgo, C., Brañas, B., Carreras, B., and Garcia, L.: Wavelet
812 Bicoherence: A New Turbulence Analysis Tool, *Phys. Plasmas*, 2, 3017–3032, 1995.
- 813 Walker, G. T., and Bliss, E. W.: World weather V, *Mem., R. Meteorol. Soc.*, 4, 53–84, 1932.
- 814
- 815 Wu, A., and Hsieh, W. W.: Nonlinear interdecadal changes of the El Niño-Southern Oscillation, *Climate Dyn.*, 21,
816 719–730, 2003.
- 817 Yun K. S and Timmermann, A.: Decadal monsoon-ENSO relationships reexamined, *Geophys Res Lett.*, 45, 2014–
818 2021, 2018.

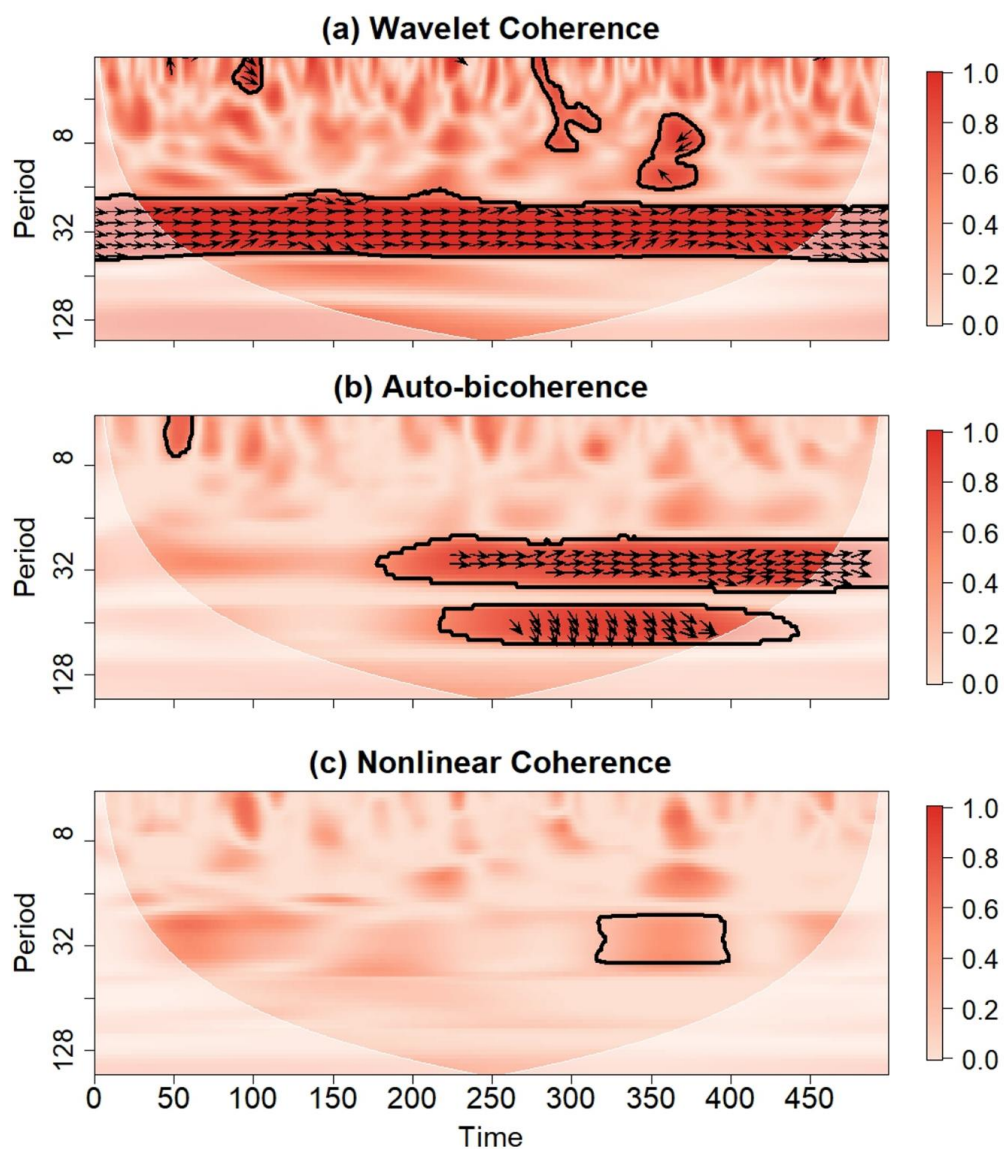


819



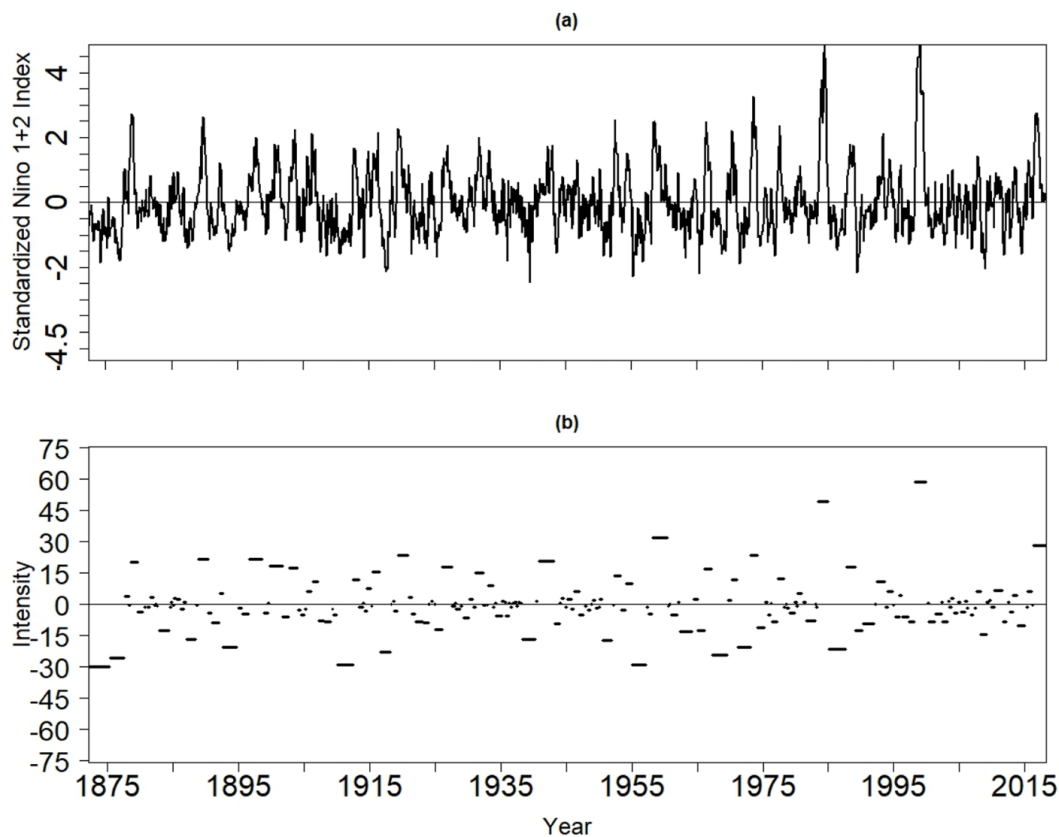
820

821 Figure 1. (a) An idealized nonlinear forcing time series together with an idealized response $R(t)$. The 120-
822 point sliding correlation between $F(t)$ and $R(t)$. (c) The 120-point sliding skewness of $F(t)$ and $R(t)$.



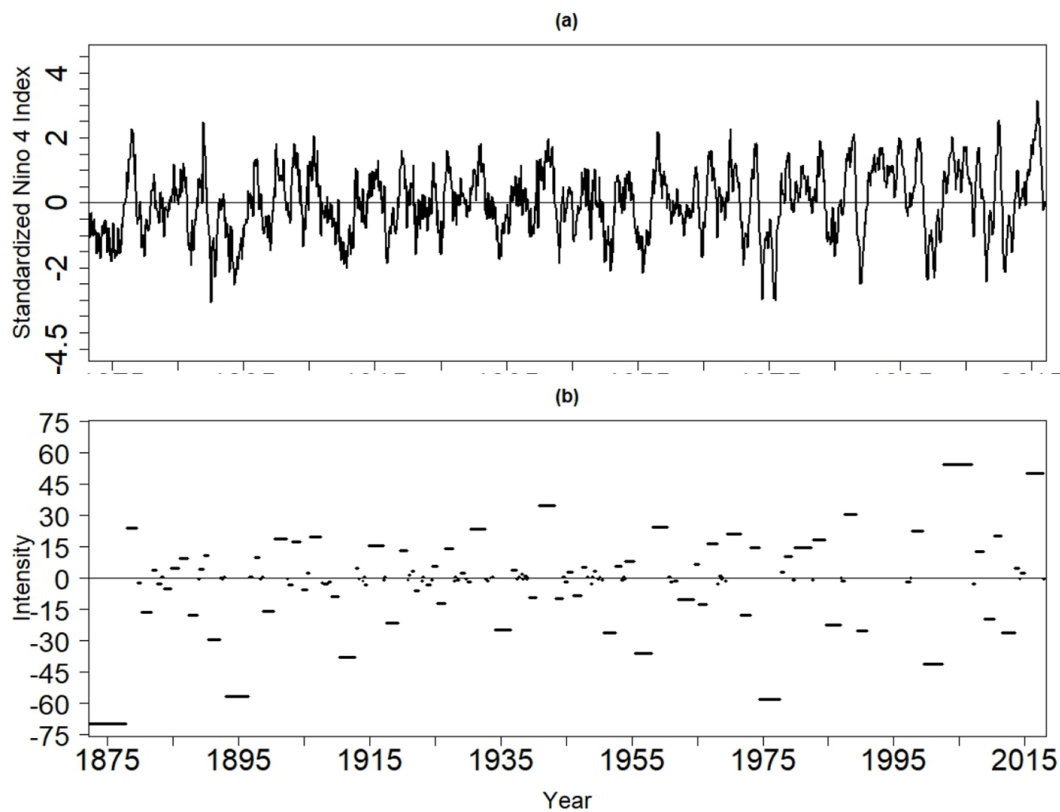
823

824 Figure 2. (a) Wavelet coherence between the time series of $F(t)$ and $R(t)$ shown in Figure 1. Arrows indicate
825 the relative phase difference, where arrows pointing to the right mean that the time series are in phase.
826 (b) The local diagonal slice of the auto-bicoherence spectrum of $F(t)$. Arrows represent the bi-phase,
827 where arrows pointing to the right mean that the phase coupling between the mode with period indicated
828 on the vertical axis and its harmonic contributes to positive skewness. (c) Nonlinear coherence between
829 $F(t)$ and $R(t)$. Contours in all panels enclose regions of 5% cumulative area-wise significance. Light-shaded
830 region represents the cone of influence where edge effects may be important.



831

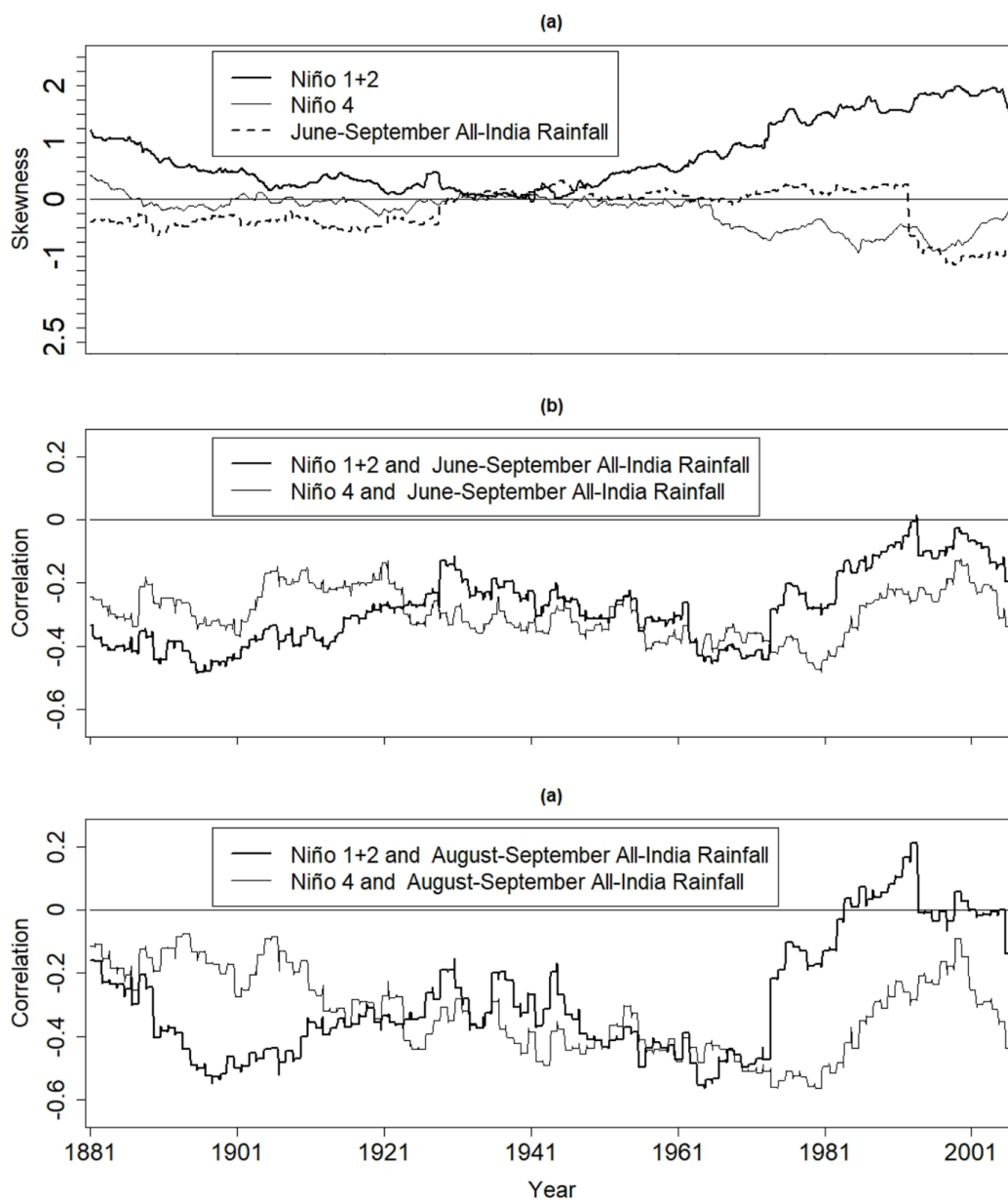
832 Figure 3. The (a) time series and (b) event spectrum of the Niño 1+2 index. The left and right end points
833 of the line segments in (b) represent, respectively, the beginning and termination of events so that the
834 length of the line segments corresponds to event persistence. The corresponding event intensity is
835 indicated on the vertical axis.



836

837 Figure 4. Same as Figure 3 but for the Niño 4 index.

838

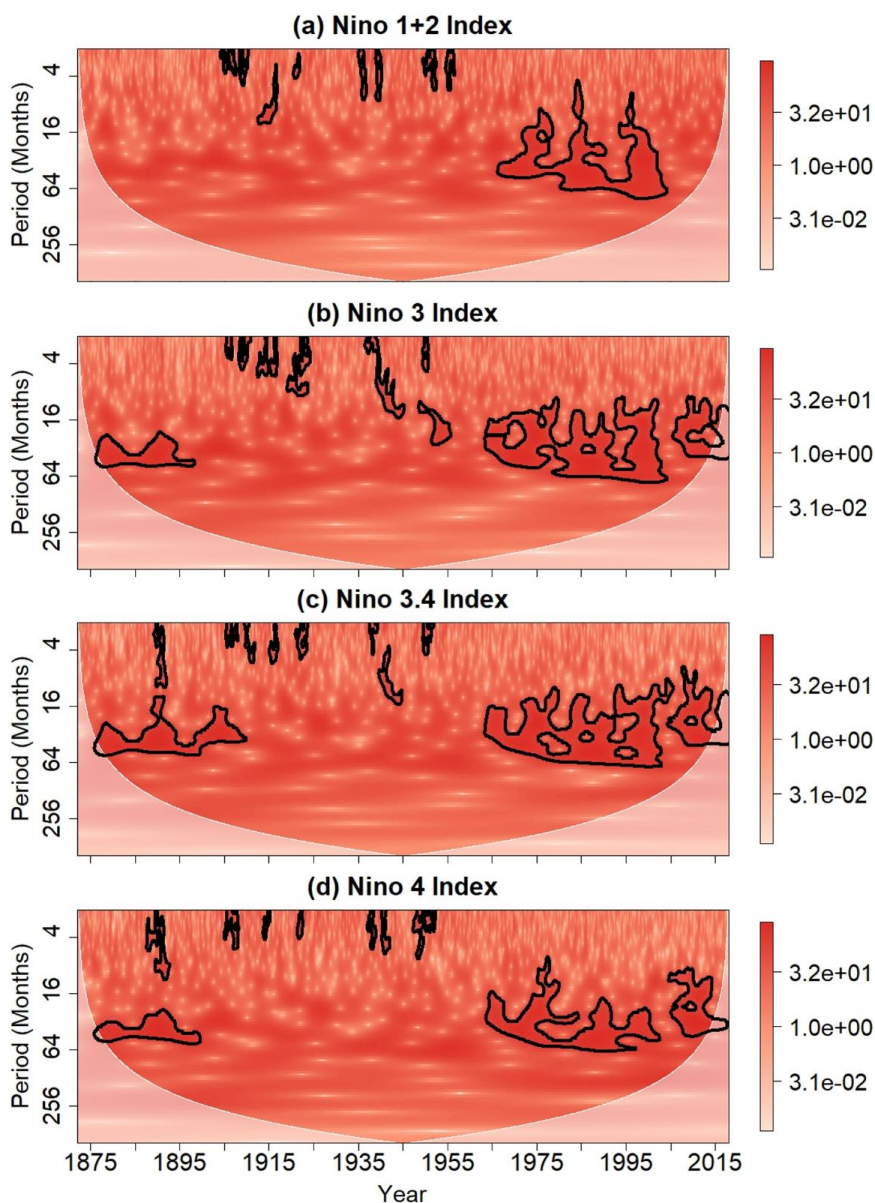


839

840 Figure 5. 20-year sliding skewness of June-September All-India rainfall and time series for the Niño 1+2
841 and Niño 4 indices. (b) 20-year sliding correlation between anomalies for June-September All-India
842 rainfall and the time series for the Niño 1+2 and Niño 4 indices. (c) Same as (b) but for August-
843 September All-India rainfall.

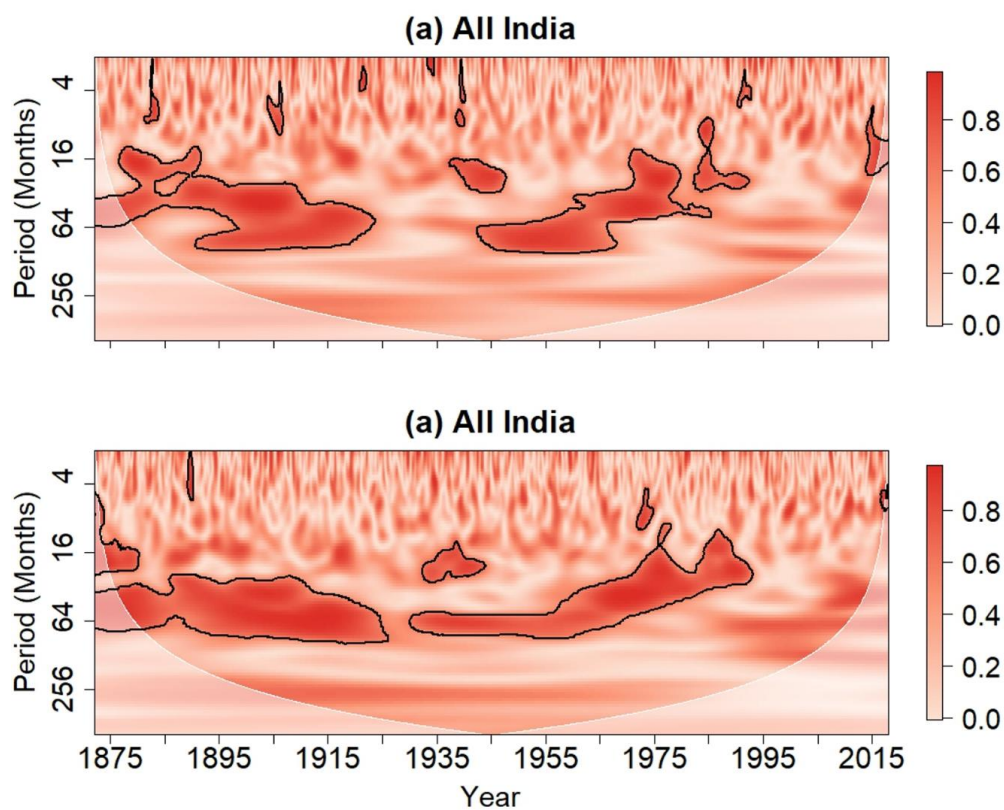


844

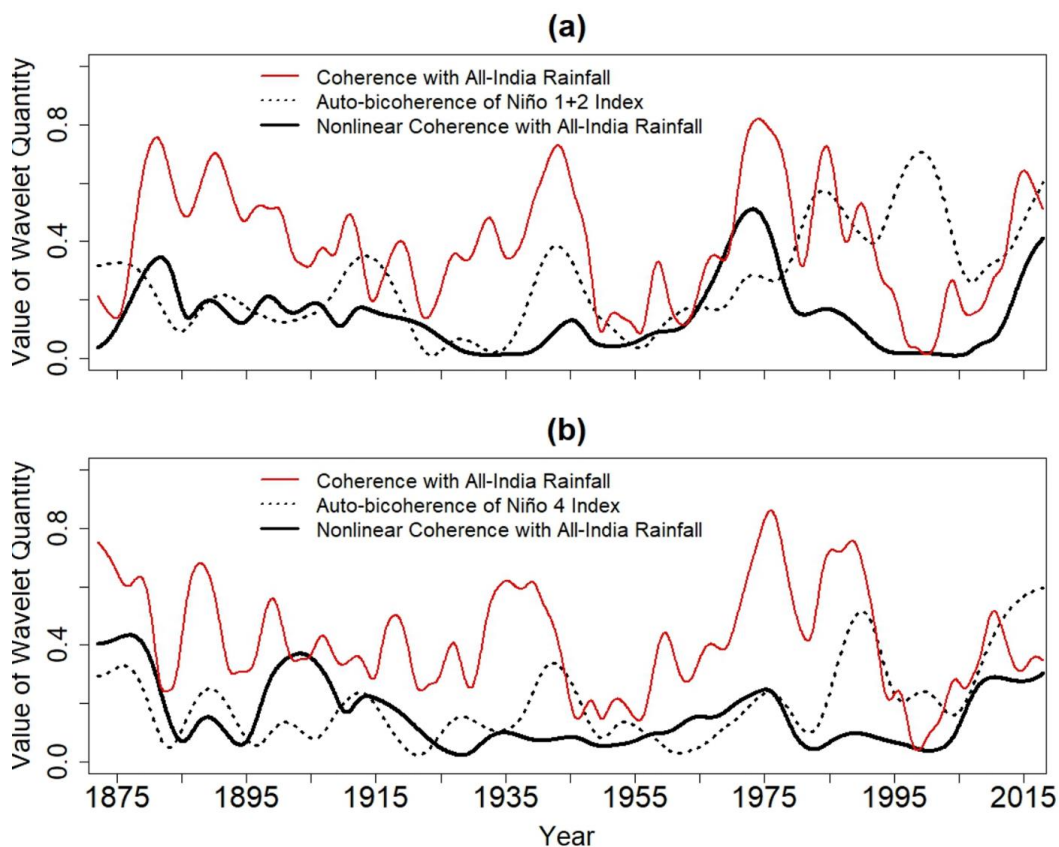


845

846 Figure 6. Wavelet Power spectrum of the (a) Niño 1+2, (b) Niño 3, (c) Niño 3.4, and (d) Niño 4 indices.
847 Contours enclose regions of 5% cumulative area-wise significance. Light-shaded region represents the
848 cone of influence, which is the region where edge effects are non-negligible.

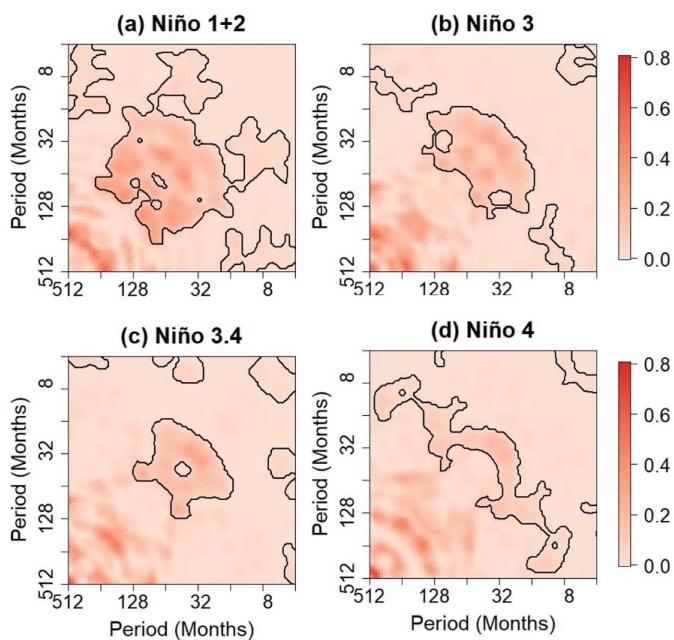


849
850 Figure 7. Wavelet coherence spectrum between All-India rainfall anomalies and time series for the (a)
851 Niño 1+2 and (b) Niño 4 indices. Contours enclose regions of 5% cumulative area-wise significance. Light-
852 shaded region represents the cone of influence, which is the region where edge effects are non-negligible.
853



854
855 Figure 8. (a) The wavelet coherence between All-India rainfall and the Niño 1+ 2 index, the auto-
856 auto-bicoherence of the Niño 1+2 index, and the nonlinear coherence between the Niño 1+2 index and All-
857 India rainfall anomalies averaged in the period band of 16 to 64 months. (b) The same as (a) but with the
858 Niño 4 index.

859

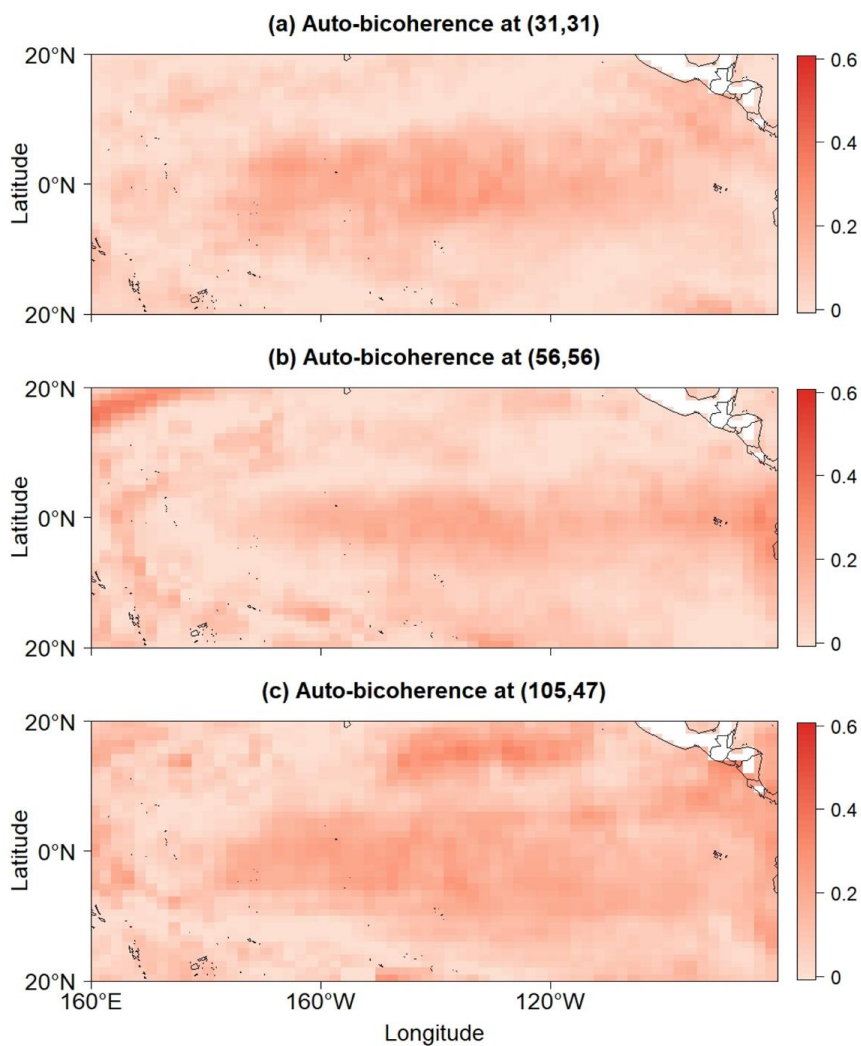


860
861

862 Figure 9. Global auto-bicoherence spectra of the (a) Niño 1+2, (b) Niño 3, (c) Niño 3.4, and (d) Niño 4
863 indices. Contours enclose regions of 5% cumulative area-wise significance.

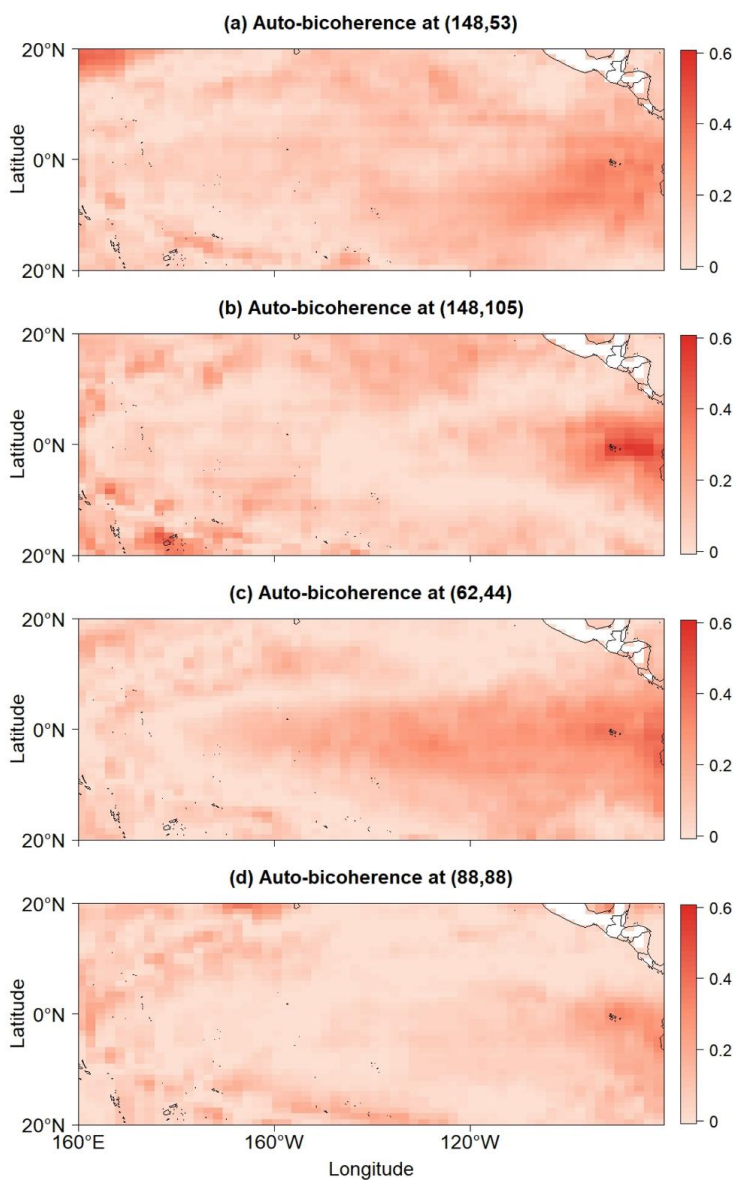
864

865



866

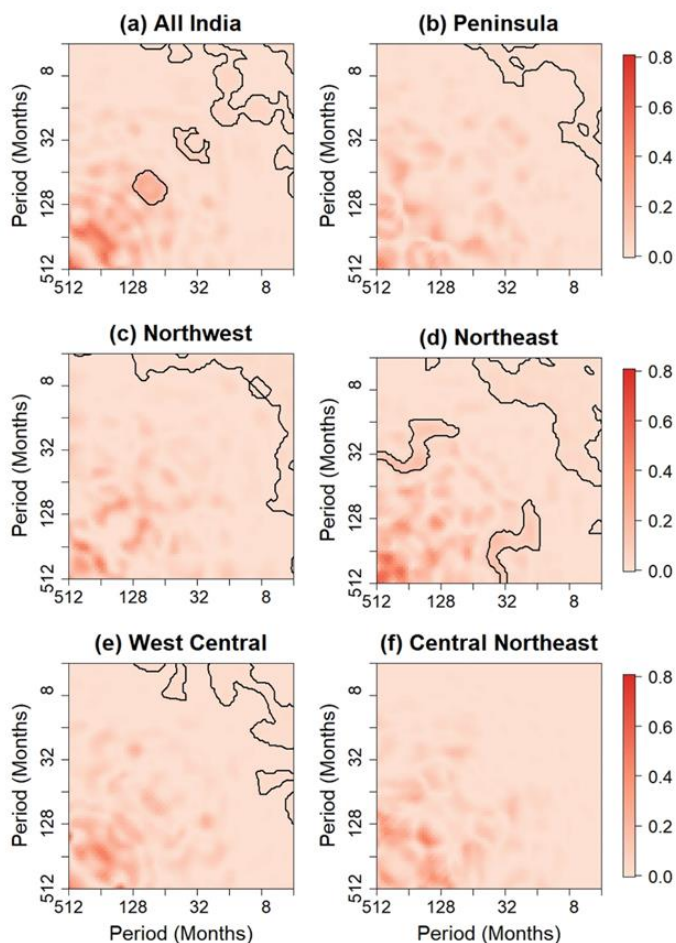
867 Figure 10. Global auto-bicoherence corresponding to the pairs (a) (31, 31), (b) (56, 56), and (c) (105, 47)
868 [months].



869

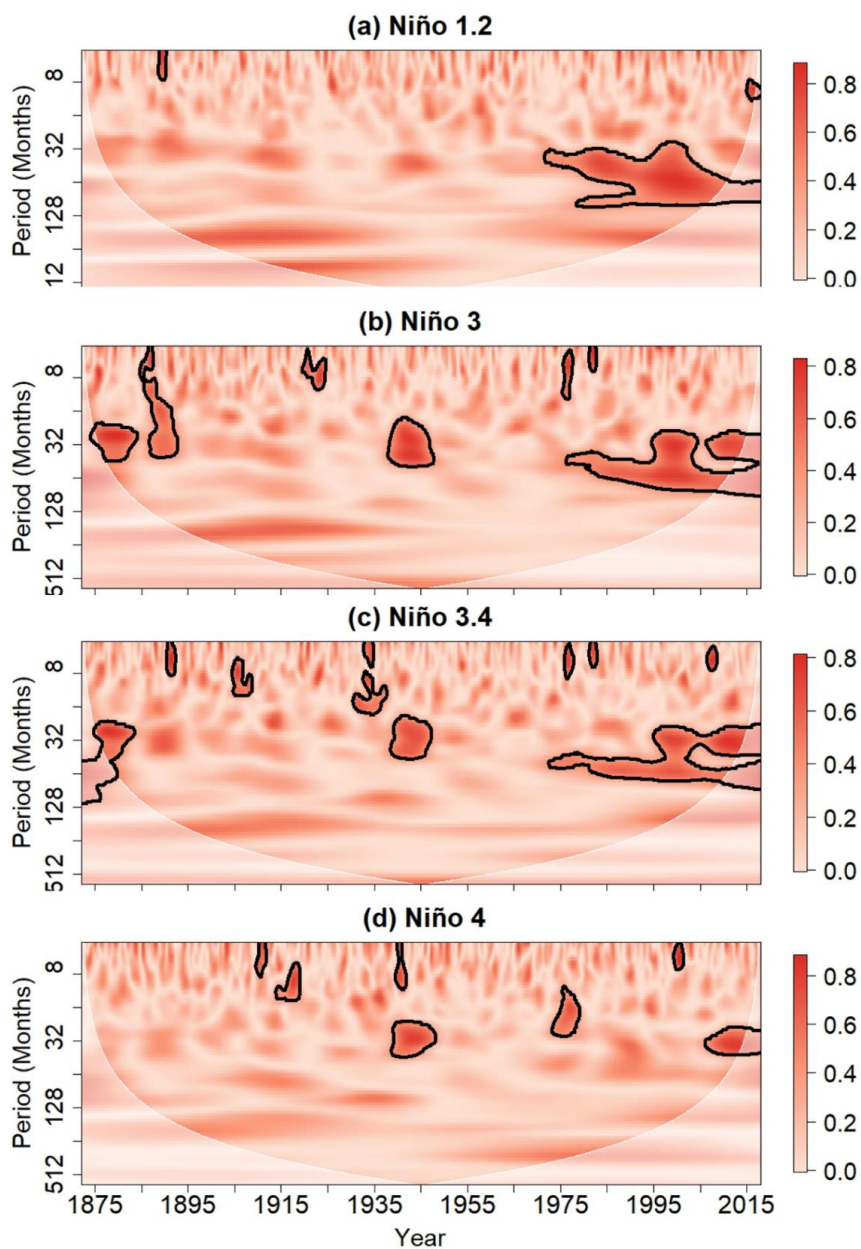
870 Figure 11. Global auto-bicoherence corresponding to the pairs (a) (158, 43), (b) (148, 105), (c) (62, 44),
871 and (d) (88,88) [months].

872



873

874 Figure 12. Global auto-bicoherence spectra of the (a) All-India, (b) Peninsula, (c) Northwest,
875 (e) West Central, and (f) Central Northeast time series. Contours enclose regions of 5% cumulative area-
876 wise significance.



877

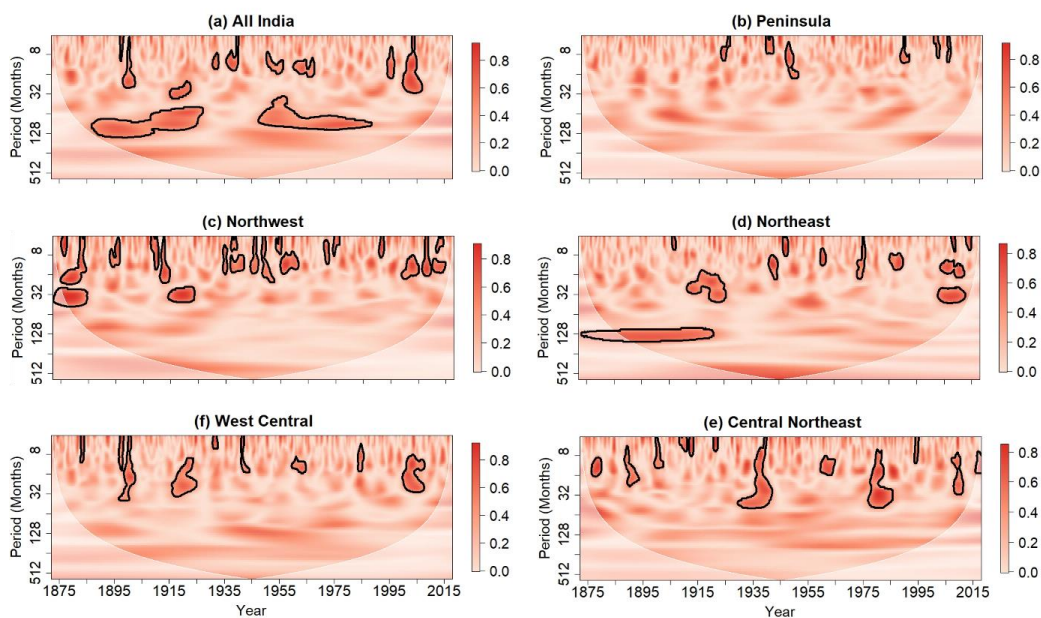
878 Figure 13. Local auto-bicoherence spectra of the (a) Niño 1+2, (b) Niño 3, (c) Niño 3.4, and (d) Niño 4
879 indices. Contours enclose regions of 5% cumulative area-wise significance and the light shading represents
880 the cone of influence.



881

882

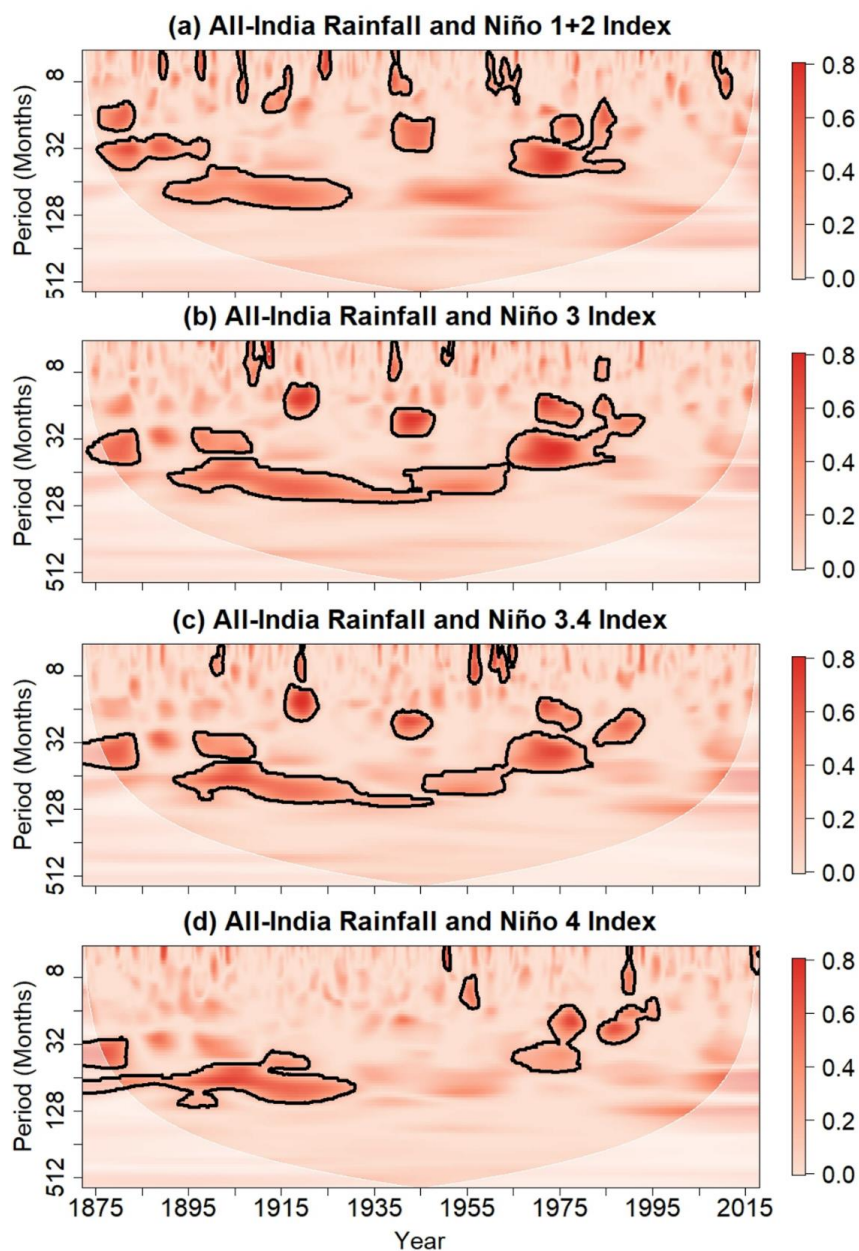
883



884

885 Figure 14. Local auto-bicoherence spectra of the (a) All-India, (b) Peninsula, (c) Northwest,
886 (e) West Central, and (f) Central Northeast time series. Contours enclose regions of the 5% cumulative
887 area-wise significance and the light shading represents the cone of influence.

888



889

890 Figure 15. Nonlinear wavelet coherence between the All-India time series and times series for the (a) Niño
891 1+2, (b) Niño 3, (c) Niño 3.4, and (d) Niño 4 indices. Contours enclose regions of 5% cumulative area-wise
892 significance and light shading represents the cone of influence.

893